

Direct numerical simulation of a three-dimensional spatially developing bubble-laden mixing layer with two-way coupling

By O. A. DRUZHININ[†] AND S. E. ELGHOBASHI

Mechanical and Aerospace Engineering Department, University of California, Irvine,
CA 92697, USA

(Received 1 July 1999 and in revised form 25 July 2000)

Direct numerical simulations (DNS) of a three-dimensional spatially-developing mixing layer (ML) laden with spherical gaseous bubbles are performed, with both one-way and two-way coupling between the two phases. Forcing is used to initialize the spanwise vortex roll-up and to create a pair of counter-rotating streamwise vortices, rendering the carrier flow three-dimensional. The characteristics of the resulting ML flow field are similar to those reported in numerous experimental and numerical studies. The volume fraction (or concentration) of the bubble phase is considered small enough to neglect bubble–bubble interactions. The no-slip fluid velocity condition is assumed at the bubble surface, and the bubble Reynolds number is less than 1 throughout the simulation time. The two-fluid formulation (TF) is used to compute the bubble-phase velocity and concentration and the two-way coupling source term in the fluid momentum equation. A Lagrangian–Eulerian mapping (LEM) solver is employed to solve the equations for the bubble velocity and concentration. LEM is capable of resolving the gradients of concentration created by the bubble preferential accumulation without numerical instabilities. Two different inflow profiles ($C_{ref}(z)$) of bubble-phase concentration are considered: a uniform profile and a tanh-profile. In the latter case, the high-speed (upper) stream is devoid of bubbles, and the low-speed (lower) stream is uniformly laden with bubbles at the inflow plane.

The DNS results show that in addition to the well-known preferential accumulation of bubbles in the vortex centres, sheets of increased bubble concentration (C -sheets) develop in the rollers created by the vortex pairing in the ML core, with two local maxima of vorticity and an enhanced strain-rate field. The development of C -sheets is governed by the stretching and contraction along the principal axes of the local strain rate.

In the case of uniform C_{ref} , the two-way coupling reduces the average ML vorticity thickness and the entrainment of the irrotational fluid into the ML core, as compared to the bubble-free case, upstream of the location of the first vortex pairing. However, both ML vorticity thickness is increased and entrainment is enhanced by the bubbles farther downstream, after the pairing. The fluid velocity fluctuations are reduced by the bubbles throughout the ML, as compared to the one-way coupling case.

In the case of the tanh-profile of C_{ref} , the velocity fluctuations and the ML vorticity thickness are increased by the bubbles upstream the location of the first vortex pairing owing to the ‘unstable’ inflow bubble stratification (Druzhinin & Elghobashi 1998).

[†] Permanent address: Applied Physics Institute, Russian Academy of Sciences, 603600 Nizhni Novgorod, Russia.

On the other hand, the velocity fluctuations are reduced by the bubbles, and the ML vorticity thickness oscillates with the streamwise distance farther downstream.

1. Introduction

Turbulent free shear flows laden with particles (solid particles, liquid droplets or gaseous bubbles) are encountered in many engineering applications. Of particular interest are the processes of particle dispersion by turbulence and the modification of the turbulence by the particles (Crowe, Gore & Trout 1985; Crowe, Chung & Trout 1993; Elghobashi 1994).

A plane mixing layer (ML) between two fluid streams of different velocities can be regarded as a canonical turbulent free shear flow (Ho & Huerre 1984). This flow has attracted the attention of many researchers owing to its relatively simple geometry which allows its laboratory implementation (Brown & Roshko 1974; Winant & Browand 1974; Breidenthal 1981; Bernal & Roshko 1986; Lasheras, Cho & Maxworthy 1986; Lasheras & Choi 1988; Koochesfahani & Dimotakis 1986), numerical simulation (Lowery & Reynolds 1986; Buell & Mansour 1989; Sandham & Reynolds 1989; Rogers & Moser 1992; Moser & Roger 1993), as well as theoretical analysis (Michalke 1964; Pierrehumbert & Widnall 1982; Corcos & Lin 1984; Corcos & Sherman 1984; Lin & Corcos 1984). These studies show that this flow provides a wealth of information about the evolution of large-scale coherent structures and their interaction with small-scale turbulence. The basic features of the ML development can be summarized as follows.

The growth of the most unstable fundamental mode, due to the Kelvin–Helmholtz instability, triggers the initial roll-up of the spanwise vortex sheet created by the velocity jump. The subsequent growth of the subharmonic mode results in pairing of the co-rotating neighbouring spanwise rollers. The growth of the spanwise rollers and their pairings are responsible for increasing the ML lateral thickness. The spanwise disturbances of the rollers (present naturally in the experiment, or prescribed in the direct numerical simulations (DNS) as an initial condition) grow and produce pairs of counter-rotating streamwise vortices. The streamwise vorticity is enhanced by the strain field in the braid zone between the consecutive spanwise rollers. The wavelength of the most unstable spanwise mode equals approximately two-thirds of the wavelength λ_x of the fundamental mode ($\lambda_x \simeq$ distance between the centres of consecutive spanwise rollers). The growth of the streamwise vortices renders ML three-dimensional, and, at sufficiently large Reynolds numbers, the flow eventually becomes fully turbulent.

There are two approaches to the numerical simulation of the mixing layer: temporally developing (TDML) and spatially developing (SDML). In TDML, the flow is periodic in the streamwise direction. This imposed periodicity results in a streamwise mean velocity profile which is antisymmetric with respect to the inflection point of that profile. This velocity profile evolves in time from a given initial condition. In SDML, which occurs naturally in a laboratory experiment and is more relevant for practical applications, the mean velocity is steady at any fixed streamwise location, and the flow field is no longer periodic in the streamwise direction. The experimental and numerical studies of SDML show that the entrainment rate of fluid from the high-speed stream into the ML core is larger than that from the low-speed stream (Dimotakis 1986; Koochesfahani & Dimotakis 1986; Lowery & Reynolds 1986). This

asymmetry is a direct consequence of the spatial development of ML. Consequently, SDML ‘bends’ towards the low-speed stream, so that the mean flow profile also becomes asymmetrical (Lowery & Reynolds 1986).

Particle dispersion in SDML has been studied experimentally by a few researchers (Lazaro & Lasheras 1992*a,b*; Crowe *et al.* 1993). These experiments show that the distribution of heavy particles is controlled by their accumulation in the streaks located in the braid zones between the spanwise rollers. Particle dispersion is enhanced in the forced ML, and is most effective for the particles whose response time is of the order of the timescale of the spanwise rollers. The measurements in SDML of gas laden with water droplets by Kiger & Lasheras (1995) show that the kinetic energy transfer between the carrier gas and droplets is inhomogeneous, and the two-way coupling process diminishes in the ML core region which is devoid of droplets owing to their preferential accumulation in the streaks. The pairing of the large-scale rollers reduces the inhomogeneity of droplet dispersion.

DNS of particle-laden, three-dimensional SDML is a challenging task since it requires the simultaneous solution of the equations of fluid motion and those of the dispersed particles. All known DNS studies of particle-laden, turbulent shear flows use the Eulerian–Lagrangian (or trajectory) approach (Elghobashi 1994). In this approach, the dispersed phase is represented by an ensemble of computational particles. Thus, the equation of motion of each computational particle is solved, and the surrounding carrier flow velocity (i.e. the fluid velocity at the instantaneous particle location) is evaluated via interpolation. This trajectory approach is computationally expensive, especially in the two-way coupling case, where a sufficient number of computational particles is required to represent the actual volume fraction of the real particles.

Crowe *et al.* (1985), Wen *et al.* (1992), Crowe *et al.* (1993), Martin & Meiburg (1994) and Crowe, Troutt & Chung (1996) considered an inviscid flow, and employed a point-vortex model to simulate the two-dimensional particle-laden TDML with one-way coupling. More recent studies employed DNS to investigate the three-dimensional TDML with one-way (Marcu & Meiburg 1996; Ling *et al.* 1998) and two-way (Miller & Bellan 1999) coupling. Numerical simulation of a bubble-laden TDML with two-way coupling was performed only in the two-dimensional case by Ruetsch & Meiburg (1994).

In a recent study, Druzhinin & Elghobashi (1998) used the two-fluid formulation (TF) to perform DNS of a decaying isotropic turbulence laden with microbubbles. In another study, Druzhinin & Elghobashi (1999) used TF to perform DNS of a bubble-laden homogeneous shear turbulent flow, and developed a Lagrangian–Eulerian mapping (LEM) solver, capable of resolving the gradients created by the preferential accumulation of microbubbles without numerical instabilities.

The objective of this paper is to perform DNS of a three-dimensional spatially developing turbulent mixing layer laden with small spherical gaseous bubbles, with one- and two-way coupling, using the two-fluid formulation. The motivation for this study is to enhance the understanding of the physical phenomena encountered in this flow. In particular, we consider two different inflow profiles of the bubble-phase concentration: a uniform profile and a tanh-profile. In the former case, the inflow bubble concentration is uniform, whereas in the latter case, the high-speed (upper) stream is devoid of bubbles and the low-speed (lower) stream is uniformly laden with bubbles.

The paper is organized as follows. The governing equations of motion of the bubble-laden flow and the numerical method are described in §2. Section 3 presents the test case of a bubble-laden Stuart vortex (with one-way coupling). The results

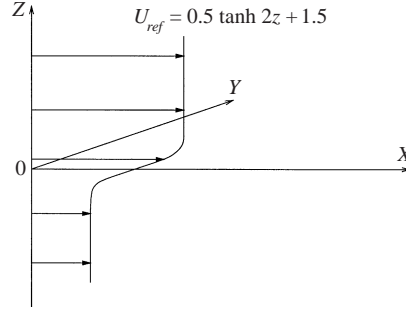


FIGURE 1. Reference frame and the inflow streamwise velocity profile for a spatially developing mixing layer.

of DNS of three-dimensional SDML with uniform inflow bubble distribution, with one- and two-way coupling, are presented in §4. The results for three-dimensional SDML with inflow tanh bubble distribution are discussed in §5. Concluding remarks are presented in §6.

2. Governing equations and numerical method

2.1. Equations of motion for a spatially developing bubble-laden mixing layer

We consider a spatially developing mixing layer with an inflow ‘reference’ dimensionless streamwise velocity profile, $U_{ref}(z)$, at $x = 0$ (see figure 1) in the form:

$$U_{ref}(z) = 0.5 \tanh 2z + 1.5. \quad (2.1)$$

All the variables in equations (2.1)–(2.8) are dimensionless via scaling by the dimensional velocity difference, $U_+^* - U_-^* = \Delta U^*$, where U_+^* and U_-^* are the dimensional velocities of the high- and low-speed streams, respectively. The corresponding dimensionless velocities are $U^+ = 2$ and $U^- = 1$, such that $U^\pm = U_{ref}(z \rightarrow \pm\infty)$, and $\Delta U = U^+ - U^- = 1$, and the dimensionless initial vorticity thickness, $\delta_{\omega 0}$, is:

$$\delta_{\omega 0} = \left. \frac{\Delta U}{dU_{ref}/dz} \right|_{z=0} = 1. \quad (2.2)$$

Spherical bubbles are injected into the mixing layer at the inflow plane. The bubble diameter, d_b , is much smaller than $\delta_{\omega 0}$. We average the equations of motion of the fluid and bubble over a lengthscale of the order of a dissipation scale, l_{diss} (to be defined below), which is much smaller than $\delta_{\omega 0}$, but much larger than the bubble diameter. Thus, the bubble phase can be treated as a continuum characterized by the velocity $V(\mathbf{r}, t)$ and concentration (volume fraction) $C(\mathbf{r}, t) = \pi d_b^3 n(\mathbf{r}, t)/6$, where $n(\mathbf{r}, t)$ is the bubble number density.

We consider two different reference profiles for the bubble concentration at the inflow plane: a uniform profile,

$$C_{ref}(x = 0) = \alpha_0, \quad (2.3)$$

or a tanh-profile,

$$C_{ref}(x = 0, z) = 0.5\alpha_0(1 - \tanh 2z), \quad (2.4)$$

where α_0 is considered small enough ($\alpha_0 \leq 10^{-2}$) to neglect the bubble–bubble interactions.

We assume that the bubble gas density, ρ_b , is negligible compared to the carrier fluid

density, ρ_f . The velocity boundary condition at the bubble surface is effectively that for a solid sphere (no-slip). We neglect the Basset and lift forces in the considered case of small bubbles (Magnaudet 1997; Druzhinin & Elghobashi 1998) whose Reynolds number is less than 1.

Thus, the governing dimensionless equations of the conservation of the momentum and mass for the fluid and bubble phases are (Druzhinin & Elghobashi 1998):

$$\frac{D\tilde{U}_i}{Dt} + U_{ref}\partial_x\tilde{U}_i + \tilde{U}_z\delta_{ix}\frac{dU_{ref}}{dz} = -\frac{1}{\rho_f}\partial_i\tilde{P} + \nu\left(\delta_{ix}\frac{d^2U_{ref}}{dz^2} + \partial^2\tilde{U}_i\right) + (C - C_{ref})g\delta_{iz}, \quad (2.5)$$

$$\partial_j\tilde{U}_j = 0, \quad (2.6)$$

$$\begin{aligned} \frac{d\tilde{V}_i}{dt} + U_{ref}\partial_x\tilde{V}_i + \tilde{V}_z\delta_{ix}\frac{dU_{ref}}{dz} = 3\left(\frac{D\tilde{U}_i}{Dt} + U_{ref}\partial_x\tilde{U}_i + \tilde{U}_z\delta_{ix}\frac{dU_{ref}}{dz}\right) \\ + \frac{1}{\tau_b}(\tilde{U}_i - \tilde{V}_i + W\delta_{iz}), \end{aligned} \quad (2.7)$$

$$\frac{dC}{dt} + U_{ref}\partial_xC = -C\partial_j\tilde{V}_j. \quad (2.8)$$

In the above equations, \tilde{U}_i and \tilde{V}_i are the deviations of the instantaneous fluid and bubble velocities from the reference profile U_{ref} , and C is the bubble concentration. The dimensionless viscosity is prescribed as $\nu = 1/Re$, where $Re = \Delta U^* \delta_{\omega 0}^* / \nu^*$ is the Reynolds number based on the dimensional velocity difference ΔU^* , the dimensional vorticity thickness $\delta_{\omega 0}^*$ and the dimensional fluid kinematic viscosity ν^* . The notations for the total derivatives are $D/Dt = \partial_t + \tilde{U}_j\partial_j$ and $d/dt = \partial_t + \tilde{V}_j\partial_j$. The bubble response time, τ_b , and the bubble terminal velocity, W , are:

$$\tau_b = \frac{d_b^2}{36\nu}, \quad (2.9)$$

and

$$W = 2\tau_b g, \quad (2.10)$$

where g is the projection of the gravity acceleration on the z -axis, $g_i = -g\delta_{iz}$. The modified pressure field, \tilde{P} , is defined as

$$\tilde{P} = P + \rho_f g \int_0^z (1 - C_{ref}) dz, \quad (2.11)$$

where P is the dynamic pressure field, and C_{ref} is given by (2.3) or (2.4). Thus, the two-way coupling term in the fluid momentum equation (2.5) is analogous to the buoyancy term, associated with the Boussinesq approximation for a stratified fluid with density $(1 - C)\rho_f$. Note that this form of the two-way coupling term is a direct consequence of neglecting the bubble material inertia for $\rho_b \ll \rho_f$, since, in this case, the viscous drag and added-mass forces are balanced by the pressure gradient and buoyancy forces (Druzhinin & Elghobashi 1998).

2.2. Numerical method for the carrier flow

Figure 1 shows the flow geometry and reference frame. In order to perform DNS in a finite computational domain which corresponds to a physical domain of infinite

extent in the vertical (z) direction, and to resolve the ML core zone with sufficient accuracy, a mapping for the z -coordinate is introduced in the form:

$$\xi = \tanh \frac{z}{8} \quad (2.12)$$

and

$$z = 4 \ln \left(\frac{1 + \xi}{1 - \xi} \right), \quad (2.13)$$

so that, for $-1 \leq \xi \leq 1$, $-\infty < z < \infty$. Thus, the partial derivatives with respect to z in equations (2.5)–(2.8) are expressed as:

$$\frac{\partial}{\partial z} = \left(\frac{1 - \xi^2}{8} \right) \frac{\partial}{\partial \xi}. \quad (2.14)$$

Accordingly, the reference velocity (2.1) and its first and second derivatives are obtained as explicit functions of ξ according to (2.12) and the equality ($\tanh 2z = 2 \tanh z / (1 + \tanh^2 z)$). The mapping (2.12) has been employed recently by Cortesi, Yadigaroglu & Banerjee (1998) in a numerical study of a stably stratified TDML.

The three-dimensional momentum conservation and continuity equations (2.5)–(2.8) are solved numerically in a parallelepiped computational domain whose dimensionless sides are $0 \leq x \leq 80$, $0 \leq y \leq 5.333$ and $-1 \leq \xi \leq 1$. Equations (2.5) and (2.6) for the fluid phase are discretized in an Eulerian framework using a second-order finite-differencing on an equispaced staggered grid containing $N_x = 480$ points in the x -direction, $N_y = 32$ in the y -direction and $N_z = 96$ in the $z(\xi)$ -direction. The Reynolds number is $Re = 400$. The integration is performed with timestep $\Delta t = 0.1 \Delta x = 1/60$.

The mean advection terms, $U_{ref} \partial_x \tilde{U}_i$, are evaluated using a second-order upwind differencing scheme, also employed by Lowery & Reynolds (1996). A second-order Adams–Bashforth scheme is used to integrate the equations in time. Pressure is obtained by solving its Poisson equation via a cosine transform with FFT (Wilhelmson & Ericksen 1977; Schumann & Sweet 1988) in the x -direction, employing FFT in the y -direction, and Gaussian elimination in the $z(\xi)$ -direction (Schmidt, Schumann & Volker 1984).

Standard periodic boundary conditions are imposed in the spanwise (y) direction for the velocity components, pressure and the bubble concentration. The Neumann's (stress-free) conditions are imposed in the $z(\xi)$ -direction according to:

$$\frac{\partial \phi}{\partial \xi} = 0, \quad \text{at } \xi = \pm 1, \quad (2.15)$$

where ϕ denotes the bubble and fluid velocities, pressure and the concentration.

Two different boundary conditions are imposed in the streamwise (x) direction at the inflow (y, z) plane, at $x = 0$, and the outflow plane, at $x = 80$.

At the inflow plane ($x = 0$), forcing is used to initialize the spanwise vortex roll-up, as proposed by Lowery & Reynolds (1986). Thus, the unsteady fluid velocity components, $U_x^f(z, t)$ and $U_z^f(z, t)$, at $x = 0$ are composed of the product of harmonic functions of time, and the eigenfunctions of the most unstable (fundamental) mode with frequency $\Omega_0 = 4/3$, and its first and second subharmonics, $\Omega_{1,2}$. The eigenfunctions are obtained by solving the two-dimensional Rayleigh-equation eigenvalue problem (see Appendix A) for each of the three frequencies $\Omega_{0,1,2}$. We follow the

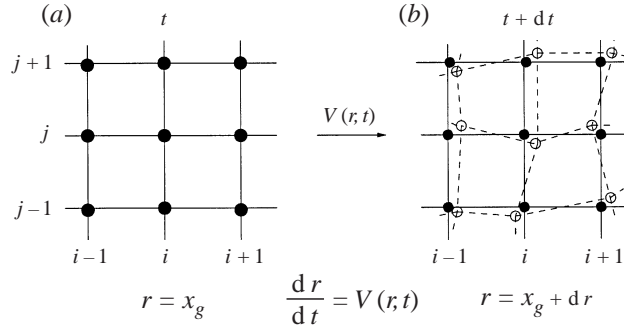


FIGURE 2. Mapping of the Eulerian grid, $r(t) = x_g$, on the Lagrangian grid $r(t + dt) = x_g + dr$. At time t the Lagrangian grid nodes (empty circles) coincide with the Eulerian grid nodes (filled circles in figure 2a). At time $t + dt$, the Lagrangian grid nodes are shifted with respect to the Eulerian grid nodes (figure 2b).

proposal of Sandham & Reynolds (1989) and include random-walk phases in the forcing functions to simulate a natural ML. All modes are forced at an amplitude of 0.02.

In order to initialize the three-dimensional flow structure we follow Buell & Mansour (1989), and supplement the inflow fluid velocity by steady components $U_y^e(y, z)$ and $U_z^e(y, z)$, created by a pair of counter-rotating Gaussian vortices with a core diameter equal to the initial vorticity thickness of the layer, $\delta_{\omega 0} = 1$, and a core vorticity 0.03 (which is 3% of the initial maximum spanwise vorticity). More details about the inflow conditions are given in the Appendix.

The inflow bubble concentration is prescribed according to the reference profile (uniform (2.3) or tanh (2.4)), and the inflow bubble velocity is set equal to the instantaneous local fluid inflow velocity.

At the outflow plane ($x = 80$), a time-dependent, advection condition is imposed as:

$$\partial_t \phi + U_a \partial_x \phi = 0, \quad (2.16)$$

where ϕ denotes the velocities \tilde{U}_i , \tilde{V}_i and concentration C . U_a is the nominal speed of the vortex structures defined by Lowery & Reynolds (1986) as $U_a = (U^+ + U^-)/2 = 1.5$, i.e. the average of the high- and low-speed stream velocities, $U^+ = 2$ and $U^- = 1$.

2.3. Lagrangian–Eulerian mapping solver for the bubble velocity and concentration

Druzhinin & Elghobash (1999) developed a Lagrangian–Eulerian mapping (LEM) solver for the integration of the equations of the bubble-phase velocity and concentration in a homogeneous shear turbulent flow. In the case of microbubbles whose diameter is less than the Kolmogorov lengthscale, the LEM solver eliminates the numerical instabilities which arise if (2.7) and (2.8) are integrated via the standard finite-difference schemes. In this section, we show how the LEM solver is implemented in the DNS of the bubble-laden three-dimensional SDML.

The objective of the LEM solver is to obtain the values of the instantaneous bubble velocity, $\tilde{V}(r, t)$, and concentration, $C(r, t)$, at the Eulerian grid nodes ($r = x_g$) (figure 2). We first integrate (2.7) and (2.8) using the LEM solver, without taking into account the advection terms associated with the reference velocity, $U_{ref} \partial_x \tilde{V}_i$ and $U_{ref} \partial_x C$. The

resulting equations are

$$\frac{d\hat{V}_i}{dt} = -\tilde{V}_z \delta_{iz} \frac{dU_{ref}}{dz} + 3 \left(\frac{D\tilde{U}_i}{Dt} + U_{ref} \partial_x \tilde{U}_i + \tilde{U}_z \delta_{iz} \frac{dU_{ref}}{dz} \right) + \frac{1}{\tau_b} (\tilde{U}_i - \tilde{V}_i + W \delta_{iz}), \quad (2.17)$$

$$\frac{d\hat{C}}{dt} = -C \partial_j \tilde{V}_j, \quad (2.18)$$

where \hat{V}_i and \hat{C} denote intermediate values of bubble velocity and concentration, respectively.

Thus, the LEM solver first evaluates the intermediate bubble-phase velocity, $\hat{V}(\mathbf{x}_g, t)$, and concentration, $\hat{C}(\mathbf{x}_g, t)$, via time integration of (2.17) and (2.18) along the characteristics $\mathbf{r}(t)$ which coincide with the trajectories of bubbles that were located at time t at the nodes of the Eulerian grid ($\mathbf{x}_g = \mathbf{r}(t)$) (see figure 2). These intermediate values, $\hat{V}(\mathbf{r}(t+dt), t+dt)$ and $\hat{C}(\mathbf{r}(t+dt), t+dt)$, are computed at the nodes of a Lagrangian grid ($\mathbf{r}(t+dt)$) coinciding with the new locations of the bubbles. Thus, the nodes of this Lagrangian grid ($\mathbf{r}(t+dt)$) are shifted with respect to the Eulerian grid nodes (\mathbf{x}_g). The displacements of the bubbles during the timestep dt from their locations at time t , at the nodes of the Eulerian grid, to the nodes of the Lagrangian grid are much smaller than the mesh size of the Eulerian grid. This small displacement allows us to evaluate the intermediate fields at the Eulerian grid nodes, $\hat{V}(\mathbf{x}_g, t+dt)$ and $\hat{C}(\mathbf{x}_g, t+dt)$, via second-order finite differencing. These solutions for the bubble velocity and concentration at the Eulerian grid nodes represent the final step in the LEM solver for a non-sheared flow (e.g. the Stuart vortex flow discussed in §3).

In the case of SDML, we have to account for the advection terms (due to the reference velocity, i.e. second term on the left-hand side of both (2.7) and (2.8)). Thus, we evaluate the bubble velocity, \tilde{V} , and concentration, C , at the upstream position from where it is advected by the mean velocity U_{ref} (in the x -direction) during the timestep dt as:

$$\tilde{V}_i = \hat{V}_i - U_{ref} \partial_x \hat{V}_i dt \quad (2.19)$$

and

$$C = \hat{C} - U_{ref} \partial_x \hat{C} dt, \quad (2.20)$$

where the gradients of \hat{V}_i and \hat{C} are evaluated via a second-order upwind differencing (Lowery & Reynolds 1986).

The DNS computations using the LEM solver, with both one-way and two-way coupling, require at least one order of magnitude less CPU-time than those using the trajectory approach.

3. Bubble dispersion in a Stuart vortex flow

As a test case of our numerical procedure, we study the dispersion of small spherical bubbles in a Stuart vortex flow with one-way coupling. The Stuart vortex flow was also used as a test simulation by Lowery & Reynolds (1986). This flow consists of a row of co-rotating vortices and may be regarded as an idealized model of a plane mixing layer (Stuart 1967). Dispersion of solid particles in the Stuart flow has been studied numerically in the one-way coupling case by Tio *et al.* (1993*a,b*) and both analytically and numerically in the two-way coupling case by Druzhinin (1995). Our objective here is to examine the performance of our numerical procedure and

compare the numerical results with an asymptotic analytical solution for the temporal development of bubble concentration at the vortex centre. For convenience, we omit in this section the tildes in the notations for the fluid and bubble velocities.

Stuart flow represents an exact two-dimensional, steady solution of the Euler equations. The local stream function of this flow, in the (x, z) -plane, can be written as:

$$\Psi(x, z) = \omega_0 \left(\frac{1 - \kappa}{1 + \kappa} \right) \ln D, \quad (3.1)$$

where

$$D = \cosh z - \kappa \cos x;$$

ω_0 is the maximum vorticity, and κ is a positive constant.

The fluid velocity components (U_x, U_z) are:

$$U_x = \frac{\partial \Psi}{\partial z} = \omega_0 \left(\frac{1 - \kappa}{1 + \kappa} \right) \frac{\sinh z}{D}, \quad (3.2)$$

$$U_z = -\frac{\partial \Psi}{\partial x} = -\omega_0 \kappa \left(\frac{1 - \kappa}{1 + \kappa} \right) \frac{\sin x}{D}. \quad (3.3)$$

The flow vorticity, ω , is in the y -direction only:

$$\omega = \frac{\partial U_x}{\partial z} - \frac{\partial U_z}{\partial x} = \omega_0 \left(\frac{1 - \kappa}{D} \right)^2, \quad (3.4)$$

In the case of $\kappa = 0$, equations (3.1)–(3.3) describe the flow $U_x = \omega_0 \tanh z$. In the limit $\kappa \rightarrow 1$ and $\omega_0(1 - \kappa) \rightarrow \Gamma$, the flow field is that created by a row of co-rotating point vortices with circulation Γ located at $z = 0$, $x = 2\pi n$, $n = 0, \pm 1, \pm 2, \dots$. In the present test case, we set $\omega_0 = 1$ and $\kappa = 0.5$.

DNS is performed for $Re = 1/\nu = 10^8$, and thus the viscous effects are negligible (cf. also Lowery & Reynolds 1986). The initial fluid velocity is prescribed by (3.2) and (3.3). The initial velocity components V_x and V_z of the bubbles are set equal to those of the local surrounding fluid,

$$V_x = U_x, \quad V_z = U_z. \quad (3.5)$$

We consider two different initial bubble distributions: a uniform distribution (2.3) and a tanh-distribution (2.4) with α_0 small enough to enable us to neglect the modification of the carrier flow by the bubbles (e.g. $\alpha_0 = 10^{-4}$). The bubble response time is set to $\tau_b = 0.1$.

DNS is performed in the domain $0 \leq x \leq 2\pi$, $0 \leq y \leq \pi/8$, $-1 \leq \xi \leq +1$ with a mesh distribution, $N_x = 64$, $N_z = 160$ and $N_y = 4$ grid points in the x -, $z(\xi)$ - and y -directions, and for dimensionless time $t \leq 25$. Although the Stuart flow studied here is essentially two-dimensional, the numerical method uses a three-dimensional-algorithm, where the flow is homogeneous in the y -direction. Accordingly, we use the minimum number of mesh points ($N_y = 4$) in the y -direction. In order to exclude the influence of gravity in this test case, we set $g = 0$ in (2.5) and (2.7).

Figure 3(a) shows the contours of the vorticity (solid lines) and bubble concentration (grey scale) in an (x, z) -plane obtained from DNS at time $t = 25$ with initial uniform bubble concentration. The figure shows that, owing to their negligible mass, but finite added-mass inertia, the bubbles accumulate at the vortex centre ($x = \pi$, $z = 0$). Consequently, the bubble concentration increases with time at the vortex centre, where the local vorticity is maximum. On the other hand, the concentration decreases

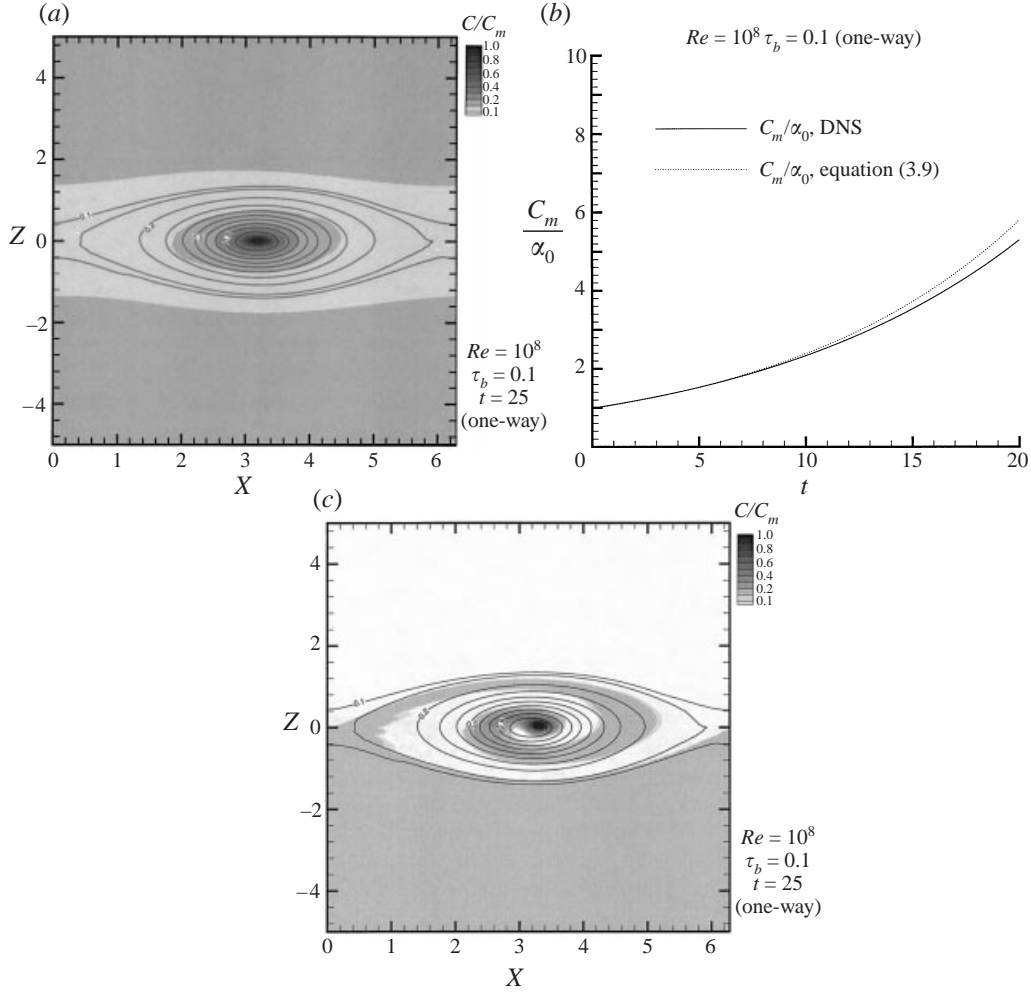


FIGURE 3. (a) Contours of the vorticity (lines) and bubble concentration (grey scale) in the Stuart flow in the (x, z) -plane at $t = 20$, for uniform initial bubble concentration, $C(t = 0) = \alpha_0$. Vorticity and concentration maxima, $\omega_m = 0.99$ and $C_m = 5.3\alpha_0$. The increments of the vorticity contours coincide with those in the table for the bubble concentration. (b) Temporal development of the maxima of the bubble concentration, C_m , in the Stuart flow (cf. figures 3a, b). (c) As in figure 3a, but for the initial bubble concentration $C(z, t = 0) = 0.5(1 - \tanh 2z)$; concentration maximum is $C_m = 3.46\alpha_0$.

in the braid region, for $x \simeq 0$, 2π , $|z| < 1$, and remains unchanged in the free-stream zone, for $|z| > 1$.

The growth of the bubble concentration at the vortex centre can be described analytically provided that the bubble response time is small compared to the flow timescale, i.e. $(\tau_b/\tau_f)^2 \ll 1$. The timescale, τ_f , in the Stuart flow is of the order $1/\omega_0 = 1$, and $(\tau_b/\tau_f)^2 \simeq (\tau_b\omega_0)^2 = 0.01 \ll 1$. In the vicinity of the vortex centre, for $x = \pi + x'$, $z = z'$ and $|x'| \ll 1$, $|z'| \ll 1$, the fluid velocity components are those of an elliptical vortex (see (3.2) and (3.3)):

$$U_x \simeq \frac{z'}{1 + \kappa}, \quad U_z \simeq -\frac{\kappa x'}{1 + \kappa}. \quad (3.6)$$

Now the approximate solution for the bubble velocity, to the leading order in τ_b , is written as (Druzhinin & Elghobashi 1998):

$$V_i = U_i + 2\tau_b \frac{DU_i}{Dt} + O\left(\frac{\tau_b^2}{\tau_f^2}\right). \quad (3.7)$$

Substituting (3.6) for the fluid velocity components into (3.7), we obtain:

$$V_x \simeq U_x - \frac{2\tau_b\kappa x'}{(1+\kappa)^2}, \quad V_z \simeq U_z - \frac{2\tau_b\kappa z'}{(1+\kappa)^2}. \quad (3.8)$$

Thus, an approximate solution of (2.8) for the maximum bubble concentration, C_m (at the vortex centre), can be written in the form:

$$C_m \simeq \alpha_0 \exp\left\{\frac{4\tau_b\kappa t}{(1+\kappa)^2}\right\}. \quad (3.9)$$

Figure 3(b) compares the temporal development of the bubble concentration at the vortex centre, $C_m(t)$, normalized by the reference concentration α_0 , obtained from the analytical solution (3.9) for $\tau_b = 0.1$ (dotted line) with that obtained from DNS (solid line). The figure shows very good agreement between the DNS results and the analytical solution (3.9) for time $t \leq 10$. At later times, a small difference arises owing to neglecting the higher-order terms in the approximate analytical solution (3.9).

Figure 3(c) shows the contours of the bubble concentration obtained from DNS of the same flow as in figure 3(a), but with the initial tanh-distribution of bubble concentration (2.4). In this case, a clockwise spiral streak of increased bubble concentration is created, extending from the braid region at $(x = 0, z = 0)$ to the vortex centre. Again, the concentration attains its maximum at the vortex centre but loses the symmetry displayed in figure 3(a). Note that layers of increased C neighbouring the layers of fluid devoid of bubbles are created owing to the entrainment of the fluid from the upper stream, which is initially devoid of bubbles, into the lower stream, which initially has uniform bubble distribution (i.e. for $z < -1$).

It is important to note that small-scale oscillations of the concentration are created in the vicinity of a hyperbolic stagnation point ($x = 0, z = 0$) (figure 3c). The development of these oscillations is caused by a complicated Lagrangian dynamics of an individual bubble in the vicinity of the flow stagnation point. The reason for this behaviour is that small perturbations of a Lagrangian tracer trajectory grow exponentially in the vicinity of the hyperbolic stagnation point of the flow (Ottino 1990). Below, we discuss a similar effect of the bubble dynamics on the development of the concentration field in the regions of SDML flow with a high local strain rate.

Comparison of the fluid velocity field (U_x, U_z) obtained from DNS at time $t = 25$ with the exact (inviscid) solution (3.2) and (3.3) shows that the maximum relative differences in the velocity components, U_x and U_z , (normalized by the free-stream velocity $|U_x|(z \rightarrow \pm\infty) = \frac{1}{3}$) are 0.01 and 0.05, respectively. This deviation from the exact solution is caused by the prescribed finite viscosity, $\nu = 1/Re = 10^{-8}$. Indeed, the difference between the exact solution and the numerical viscous solution is evaluated as $\Delta U \simeq \sqrt{\nu t}/\Delta t$. Thus, for timestep $\Delta t = 0.01$, we obtain $\Delta U \simeq 0.05$ for time $t = 25$, which is of the order of (even somewhat larger than) the observed absolute differences, $\Delta U_x = 0.003$ and $\Delta U_z = 0.015$. However, at later times the viscous effects result in the vorticity roll-up, so that the flow becomes unsteady.

We have also performed DNS of a Stuart vortex in the lateral (y, z) -plane, with prescribed initial fluid velocity components U_y and U_z , and uniform constant $U_x = 1$ and initial bubble concentration. Comparing these DNS results with the analytical solution (3.9) for the maximum concentration and the exact solution (3.2), (3.3) for the fluid velocity shows agreement similar to that of the Stuart vortex in the (x, z) -plane.

Therefore, the DNS results of the bubble-laden Stuart vortex flow discussed above show that our numerical procedure with the mapping $z(\xi)$ (2.12) and the LEM solver reproduces the flow dynamics with sufficient accuracy, and resolves the gradients of bubbles concentration created by the preferential accumulation.

4. Three-dimensional SDML with uniform bubble concentration

In this section, we present the results of DNS of a bubble-laden, three-dimensional, spatially developing forced mixing layer, with both one- and two-way coupling, and a uniform bubble concentration (2.3) at the inflow plane.

4.1. Bubble-laden three-dimensional SDML with one-way coupling

4.1.1. Instantaneous flow field

Initially, the deviations \tilde{U}_i ($i = x, y, z$) of the instantaneous fluid velocity field from the reference velocity, U_{ref} , are set equal to zero throughout the computational domain. In order to minimize the influence of the initial conditions, we first compute only the fluid flow (equations (2.5) and (2.6)) until time $t = 60$. By this time, the initial flow field is ‘washed’ out of the computational domain by the mean advection, and the carrier flow can be regarded as nearly stationary. At $t = 60$, we inject the bubbles into the flow, and start solving (2.7) and (2.8) in addition to (2.5) and (2.6).

The initial bubble concentration is uniformly constant throughout the computational domain, $C(t = 60) = \alpha_0$, and is assumed small enough (e.g. $\alpha_0 = 10^{-4}$) for us to neglect the influence of the bubbles on the carrier flow (one-way coupling). Thus, the source term in the fluid momentum equation (the last term on the right-hand side of (2.5)) is set equal to zero.

The dimensionless bubble response time is prescribed as $\tau_b = 0.05$, and the dimensionless bubble diameter is $d_b = (36\nu\tau_b)^{1/2} \simeq 0.067$, where $\nu = 1/Re$ and $Re = 400$, so that $d_b \ll \delta_{\omega 0} = 1$.

In order to show that the values of the physical parameters in our DNS are similar to those in a typical laboratory experiment, we calculate the dimensional velocity difference and vorticity thickness, ΔU^* and $\delta_{\omega 0}^*$:

$$\Delta U^* = \left(\frac{g^*}{g} \nu^* Re \right)^{1/3}, \quad \delta_{\omega 0}^* = \left(\frac{g}{g^*} \right)^{1/3} (\nu^* Re)^{2/3}, \quad (4.1)$$

where g is the dimensionless acceleration due to gravity, prescribed as $g = 1$, and ν^* and g^* are the dimensional fluid kinematic viscosity and gravitational acceleration. Therefore, substituting $g^* = 980 \text{ cm s}^{-2}$, and $\nu^* = 0.01 \text{ cm}^2 \text{ s}^{-1}$ (for water at room temperature) in (4.1) gives the dimensional vorticity thickness $\delta_{\omega 0}^* \simeq 0.25 \text{ cm}$ and velocity difference $\Delta U^* \simeq 16 \text{ cm s}^{-1}$. The dimensional bubble diameter is $d_b^* = d_b \delta_{\omega 0}^* \simeq 170 \mu\text{m}$. These parameters are of the order of those in typical laboratory bubble-laden flows (cf. experiments by Rightley 1995).

The dimensionless dissipation lengthscale of the flow, l_{diss} , can be estimated as $l_{diss} \simeq (2\pi/Re \omega_{max})^{1/2}$. The maximum vorticity is of the order $\omega_{max} \simeq 1$ throughout the simulation, so that $l_{diss} \simeq 0.13$. Thus, for the given grid cell size ($\Delta x = \Delta y =$

$\Delta z(z=0) = \frac{1}{6}$) in each coordinate direction (x, y, z) , the product $l_{diss}k_{max} \simeq 2.5$, where k_{max} is the maximum resolved wavenumber ($k_{max} = \pi/\Delta x$). This means that the smallest scales of the fluid motion are well resolved in our DNS (cf. Yeung & Pope 1988).

Since the bubble diameter is smaller than the flow dissipation scale, and much smaller than the initial layer vorticity thickness, $d_b \ll l_{diss} \ll \delta_{\omega 0}$, the conditions needed for deriving the two-fluid formulation are satisfied. For the considered bubble diameter, the bubble Reynolds number remains less than 1 throughout the simulation. The conditions $Re_b < 1$ and $d_b \ll l_{diss}$ are consistent with the assumptions used in deriving the bubble equation of motion (2.7) (Druzhinin & Elghobashi 1998).

The initial bubble velocity at any location is set equal to the local instantaneous fluid velocity:

$$\tilde{V}_i = \tilde{U}_i. \quad (4.2)$$

The simulation is continued until time $t = 160$.

Figure 4(a) shows the instantaneous contours (in colour) of the y -component of the vorticity, ω_y , in an (x, z) plane at a spanwise location $y = 2.67$, at times (i) $t = 150$, (ii) $t = 155$ and (iii) $t = 160$. This vorticity, ω_y , is obtained from the instantaneous fluid velocity field \tilde{U}_i according to:

$$\omega_y = \frac{dU_{ref}}{dz} + \partial_z \tilde{U}_x - \partial_x \tilde{U}_z. \quad (4.3)$$

Forcing at the fundamental mode frequency, Ω_0 , enhances the roll-up of the spanwise vorticity, whereas forcing at the frequencies Ω_1 and Ω_2 speeds up the growth of subharmonics and the vortex pairing process. The figure shows that the vortex pairing, enhanced by the forcing at the subharmonic frequency Ω_1 , occurs at $30 \leq x \leq 40$. This is in agreement with the results of Lowery & Reynolds (1986) who used the same reference velocity profile (2.1) and forcing at the same frequencies $\Omega_{0,1,2}$. However, in our DNS, the streamwise location of the pairing fluctuates in time, since the phases of the forcing modes are random-walked (cf. Appendix A). The growth of the first subharmonic mode increases the streamwise lengthscale (measured by the distance between the centres of consecutive spanwise rollers) from $\lambda_x \simeq 7$, the lengthscale of the fundamental mode, at $x \simeq 30$, to $\lambda_x \simeq 10$ at $x \simeq 60$ (after the vortex pairing). Comparing the locations of the rollers at three different times in figure 4(a) shows that the rollers are advected with velocity $U_a = 1.5$. Note also that the vortices exit the domain naturally, without being distorted, thus confirming the accuracy of the advection boundary condition (2.16) at the outflow plane ($x = 80$).

Figure 4(b) shows the instantaneous bubble concentration contours in an (x, z) -plane, normalized by the maximum concentration in that plane, at the same y -location and times as figure 4(a). The figure shows that bubbles, owing to their added-mass inertia (Maxey 1987), accumulate in the centres of the spanwise (ω_y) rollers (cf. blue for local maxima of C and ω_y in figures 4(a) and 4(b)). The figure also shows that the preferential bubble accumulation creates streaks of fluid devoid of bubbles (magenta) extending from the braid zones ($x \simeq 40$, $x \simeq 54$ and $x \simeq 64$) to the peripheries of the rollers ($x \simeq 50$, $x \simeq 60$ and $x \simeq 70$ in figures 4(a)(iii) and 4(b)(iii) at time $t = 160$). On the other hand, C remains uniform (yellow in figure 4(b)) in the irrotational flow region ($|z| \geq 5$). This structure of the concentration field is similar to that in the bubble-laden Stuart vortex flow (figure 3a). However, the sequence of streaks becomes more complex downstream, as the spanwise rollers grow in size (cf. rollers at $x \simeq 50$, 60 and 70 in figure 4(a)(iii) and the concentration field in figure 4(b)(iii)).

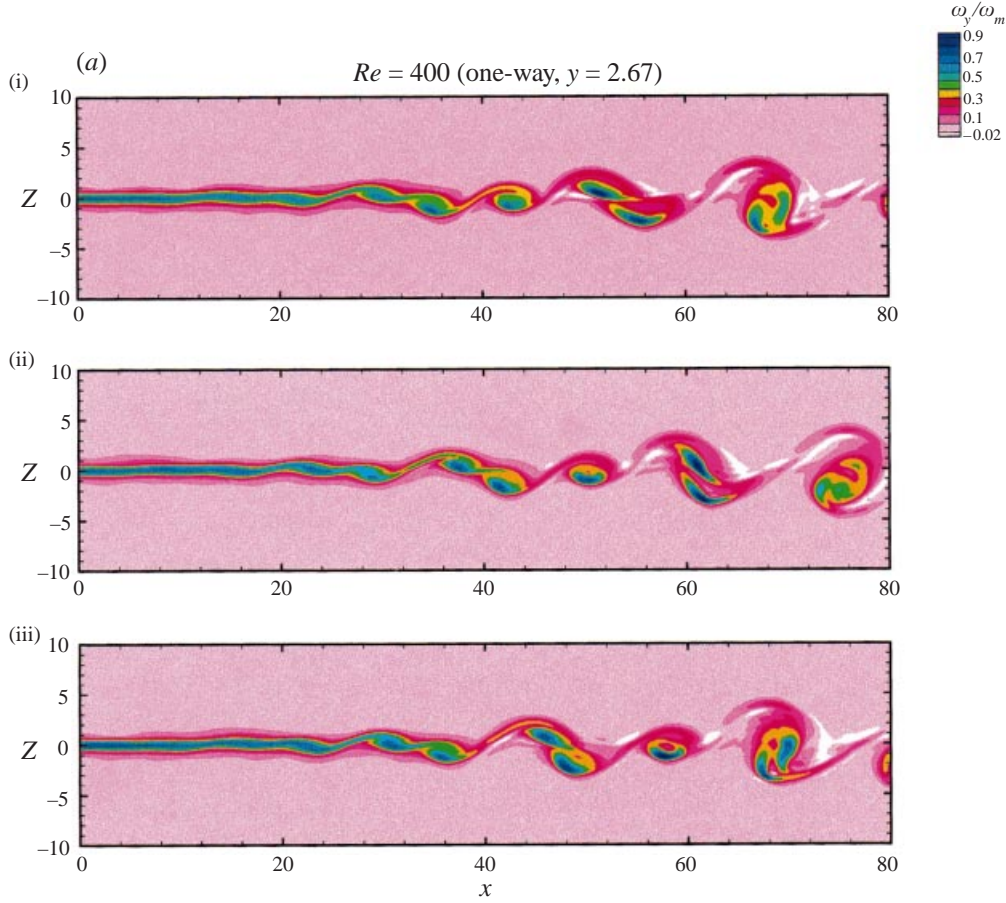


FIGURE 4 (a). For caption see page 41.

Comparison of the bubble-phase concentration distribution inside the centres of the spanwise rollers at different times (cf. figures 4(i), 4(ii) and 4(iii) with $t = 150, 155$ and 160 , respectively) shows that the growth of C in the vortex centres is accompanied by the creation of sheet-like patterns of increased C in the rollers consisting of two corotating vortices. For example, compare the rollers at locations $x \simeq 48$, $x \simeq 58$ and $x \simeq 70$ in figures 4(a)(iii) and 4(b)(iii). On the other hand, there are no sheets of increased C in the rollers where the flow is dominated by a single ω_y -vortex (for example, the roller at $x \simeq 76$ at $t = 155$, figures 4(a)(ii) and 4(b)(ii)). We discuss this point in more detail below.

SDML becomes three-dimensional owing to the development of the streamwise vortices (Lasheras *et al.* 1986). The evolution of these streamwise (ω_x) vortices (also denoted as ‘ribs’ (Hussain 1983; Buell & Mansour 1989; Rogers & Moser 1992) has been studied in detail both experimentally by Bernal & Roshko (1986), Lasheras *et al.* (1986) and Lasheras & Choi (1988), and numerically by Buell & Mansour (1989) and Rogers & Moser (1992). The primary mechanism governing their development is the stretching of the streamwise vortex lines in the braid regions between the consecutive spanwise rollers. In our DNS, these vortices are created by the inflow boundary condition (cf. Appendix A).

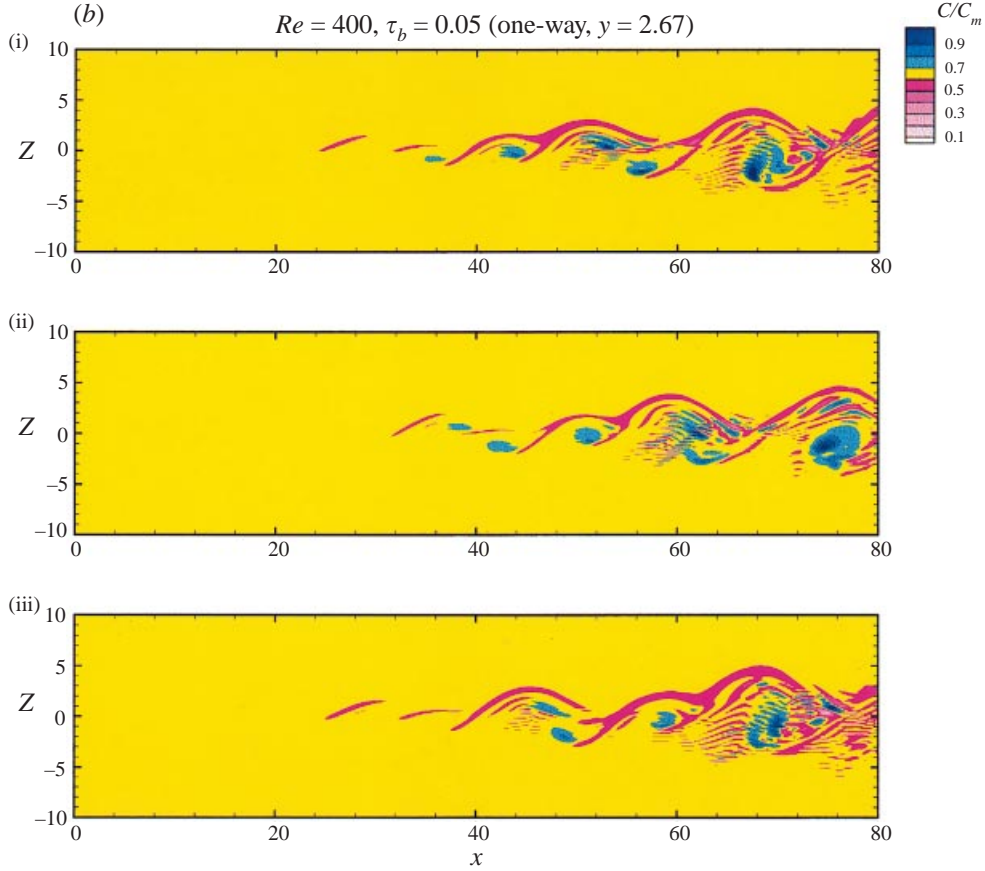


FIGURE 4 (b). For caption see page 41.

In order to examine the three-dimensional structure of three-dimensional bubble-laden SDML, we plotted in figures 4(c) and 4(d) the instantaneous iso-surfaces of the enstrophy ($\omega^2 = 0.1$) and bubble concentration ($C = 1.2\alpha_0$) in the domain $40 \leq x \leq 80$, $0 \leq y \leq 5.333$ and $-6.5 \leq z \leq 6.5$ at time $t = 160$. Note that since $\omega^2 = \sum_{i=x,y,z} \omega_i^2$, $\omega^2 \simeq \omega_x^2$, if $\omega_x^2 \gg \omega_y^2, \omega_z^2$, and $\omega^2 \simeq \omega_y^2$, if $\omega_y^2 \gg \omega_x^2, \omega_z^2$, respectively. Thus, the iso-surface of ω^2 coincides with that of ω_y^2 inside the spanwise rollers (where $\omega_y^2 \gg \omega_x^2, \omega_z^2$), whereas the iso-surface of ω^2 coincides with that of ω_x^2 in the vicinity of the streamwise ribs in the braid region between the rollers (where $\omega_x^2 \gg \omega_y^2, \omega_z^2$). The chosen value of the enstrophy ($\omega^2 = 0.1$) is close to the maxima of ω_x^2 in the ribs at $x = 58$ and $x = 68$. Thus, the iso-surface in figure 4(c) shows both the structure of the ω_y -rollers ($x \simeq 50, 60$ and 70 in figure 4a(iii)), where $\omega^2 \simeq \omega_y^2 \gg \omega_x^2$, and that of the ω_x -ribs (where $\omega^2 \simeq \omega_x^2 \gg \omega_y^2$).

Figure 4(d) shows the iso-surface of the bubble concentration $C = 1.2\alpha_0$. The figure shows that bubbles accumulate in the centres of the ω_y -rollers, located at $x \simeq 50, 60$ and 70 , and that the bubble concentration is reduced in the region between the ribs owing to a higher strain and pressure, as shown by Lasheras *et al.* (1986), and is increased in the centres of the ribs with higher enstrophy. As a result, a cylindrical ‘dumb-bell’ pattern of increased concentration is created inside the spanwise roller at $x \simeq 60$.

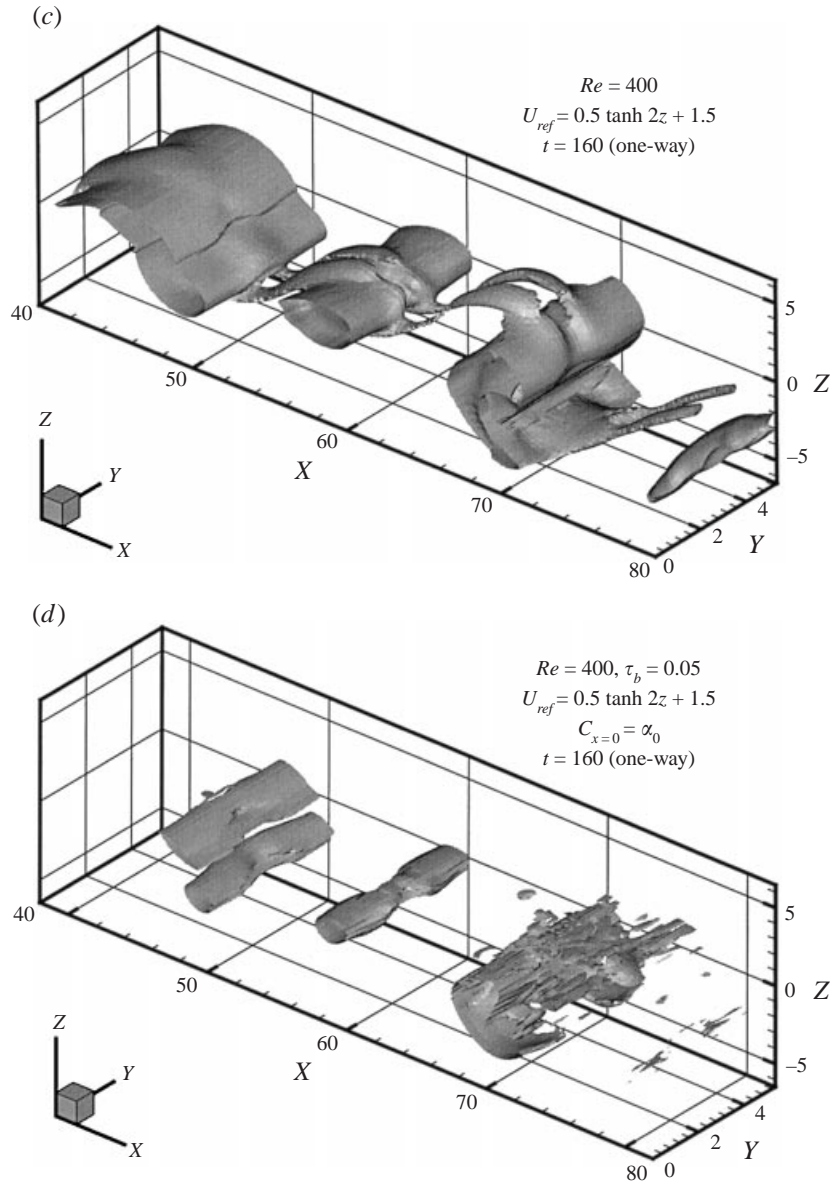


FIGURE 4 (c, d). For caption see page 41.

In order to examine the local flow field in more detail, we plot in figures 4(e) and 4(f) the cross-sections of the streamwise vorticity and bubble concentration by (y, z) -planes at $x = 68$, $t = 160$. The figures show that the bubbles accumulate in spanwise sheets and also in the centres of streamwise vortices (patches of positive and negative ω_x in figure 4e). At the same time, the concentration, C , is reduced in the region of higher strain between the ω_x -vortices.

Figures 4(b) and 4(d) show that bubbles accumulate in spanwise sheets inside the ω_y -roller at $x \simeq 70$. On the other hand, in the roller located at $x \simeq 76$ at time $t = 155$ (figure 4a(ii)) the sheets of the bubble concentration are not created (cf. figure 4b(ii))

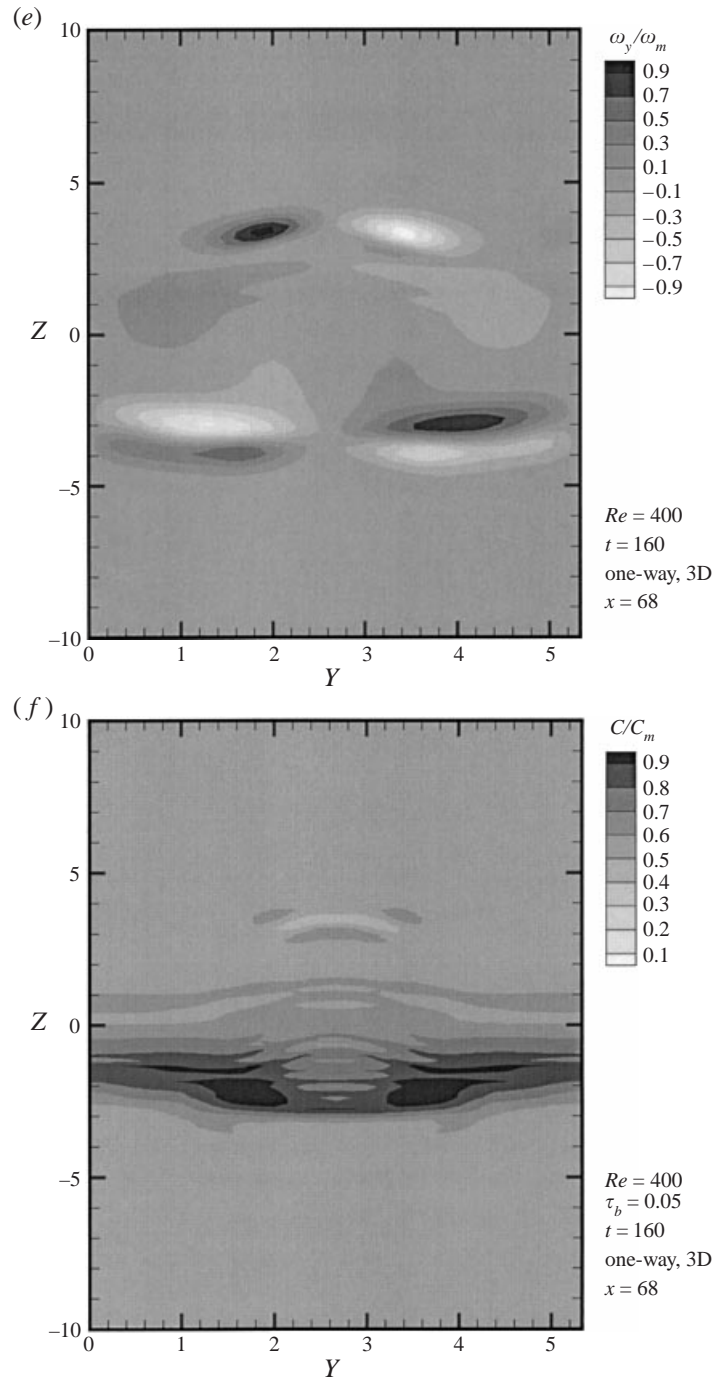


FIGURE 4 (e,f). For caption see page 41.

at $x \simeq 76$). We explain below the reason for this difference in the local structure of the bubble concentration field.

The sheet-like patterns of the concentration (C -sheets) are created owing to the combined effects of the bubbles (added-mass) inertia, buoyancy and the local structure

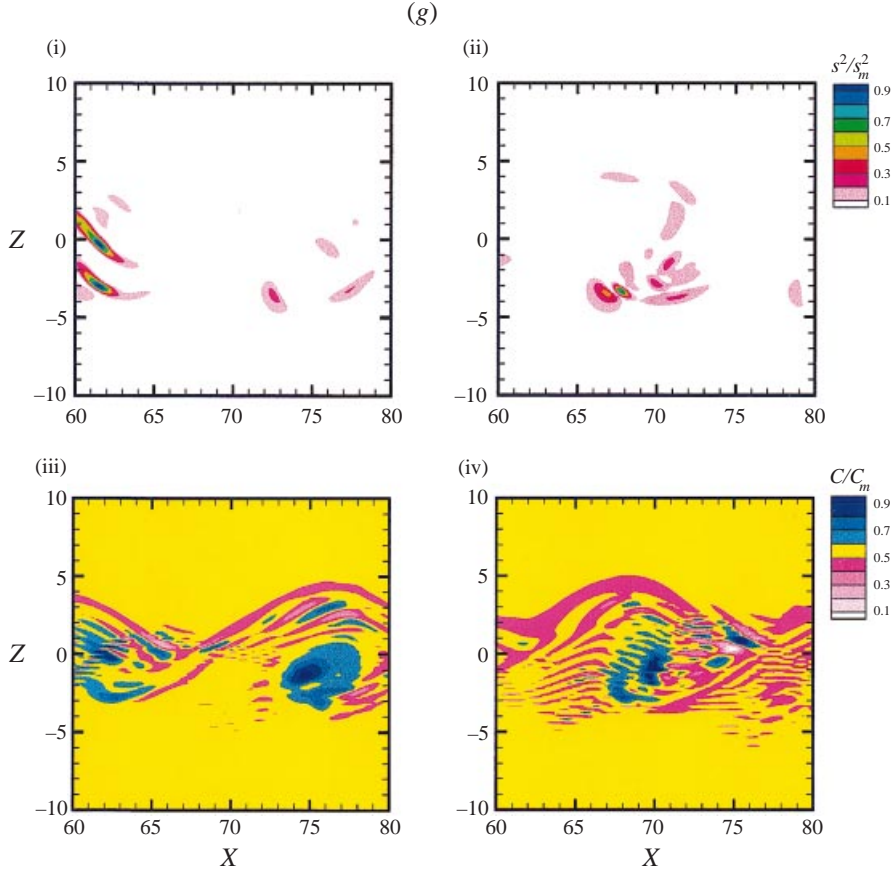


FIGURE 4 (g). For caption see page 41.

of the flow in a ω_y -roller (for example, the roller at $x \simeq 70$, figure 4a(iii)). The added-mass inertia of the bubbles causes their preferential accumulation at the centres of ω_y -vortices (cf. blue regions for both ω_y and C in figure 4b). Buoyancy, on the other hand, causes an upward displacement of the bubbles from the regions of large ω_y , thus reducing the effect of their preferential accumulation. Thus, both the preferential accumulation and buoyancy contribute to the local growth of the concentration gradients.

In order to explain why the C -sheets are created inside the roller at $x \simeq 70$ and $t = 160$ (figure 4a(iii)), while there are no C -sheets inside the roller at $x \simeq 76$ and $t = 155$ (figure 4a(ii)), we plot in figure 4(g) the contours of the sum, s^2 , of the squares of the symmetric components of the strain rate tensor in the x - and z -directions, $\partial_x U_x$ and $\partial_z U_z$:

$$s^2 = (\partial_x U_x)^2 + (\partial_z U_z)^2, \quad (4.4)$$

evaluated at streamwise locations $60 \leq x \leq 80$ and times $t = 155$ (figure 4g(i)) and $t = 160$ (figure 4g(ii)). Figures 4(g)(iii) and 4(g)(iv) show the corresponding contours of the bubble concentration at the same streamwise locations and times as figures 4(g)(i) and 4(g)(ii).

Now, figure 4(a)(iii) shows that there are two local maxima of ω_y -vorticity in the roller located at $x \simeq 70$ at $t = 160$. At an earlier time ($t = 155$), this roller was located

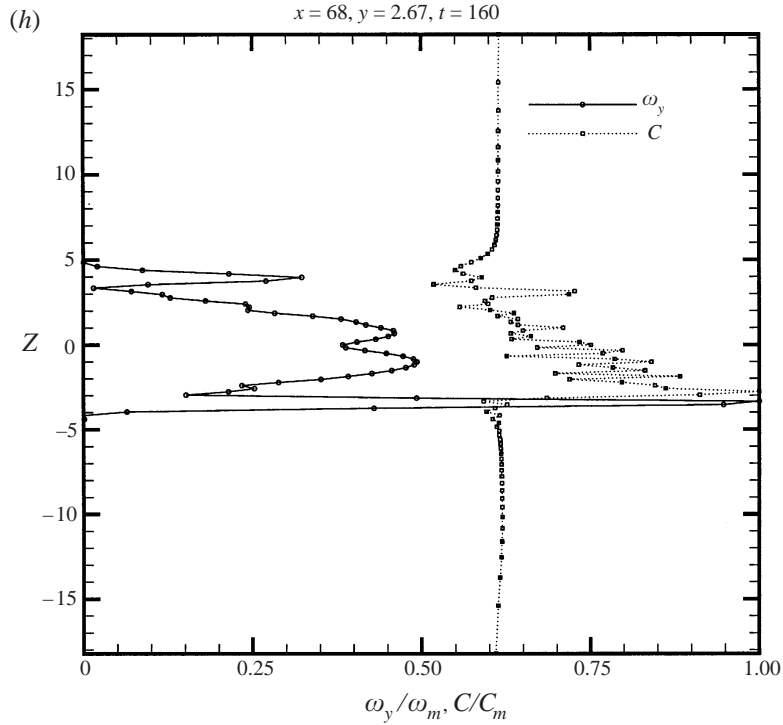


FIGURE 4. (a) ω_y -vorticity contours in the (x, z) -plane at $y = 2.67$ of the three-dimensional spatially developing mixing layer at different times, (i) $t = 150$, (ii) $t = 155$ and (iii) $t = 160$. Vorticity maxima are $\omega_m = 1.34, 1.35$ and 1.29 , respectively. (b) Bubble concentration contours in the (x, z) -plane at $y = 2.67$ of the three-dimensional SDML at different times, (i) $t = 150$, (ii) $t = 155$ and (iii) $t = 160$. Concentration maxima are (i) $C_m = 1.74\alpha_0$, (ii) $C_m = 1.88\alpha_0$ and (iii) $C_m = 1.92\alpha_0$, respectively. (c) Iso-surface of the flow enstrophy, $\omega^2 = 0.1$, of the three-dimensional SDML at time $t = 160$. (d) Iso-surface of the bubble concentration, $C = 1.2\alpha_0$, of three-dimensional SDML at time $t = 160$. (e) ω_x -vorticity contours in (y, z) -plane at $x = 68$ of three-dimensional SDML at time $t = 160$. Maximum vorticity $\omega_m = 0.41$. (f) Bubble concentration contours in the (y, z) -plane at $x = 68$ of the three-dimensional SDML at time $t = 160$. Maximum concentration $C_m = 1.74\alpha_0$. (g) Contours of the strain rate, s^2 , and bubble concentration, C , in the (x, z) -plane at $y = 2.67$ of the three-dimensional SDML at (i)(iii) $t = 155$ ($s_m^2 = 0.31$, $C_m = 1.78\alpha_0$), and (ii)(iv) $t = 160$ ($s_m^2 = 0.19$, $C_m = 1.92\alpha_0$). (h) z -profiles of the ω_y -vorticity component and bubble concentration, C , normalized by their respective local maximum values, $\omega_m = 0.99$ and $C_m = 1.63\alpha_0$, at $x = 68$, $y = 2.67$ and $t = 160$.

upstream at $x \simeq 62$ (cf. ω_y -patches of blue in figures 4a(ii) and 4a(iii)). Figures 4(a)(ii), 4(a)(iii), 4(g)(i) and 4(g)(ii) show also that there is a region of reduced vorticity and enhanced strain rate between the ω_y -maxima at $x \simeq 62$, $-3 < z < 2$ ($t = 155$) and $x \simeq 68$, $-4 < z < 1$ ($t = 160$). Figures 4(g)(iii) and 4(g)(iv) show that sheets of the increased concentration, C , are created inside this roller at the same locations of large s^2 in figures 4(g)(i) and 4(g)(ii). On the other hand, figure 4(a)(ii) shows that the flow inside the neighbouring roller, located at $x \simeq 76$ and $t = 155$, is dominated by a single ω_y -vortex, and figure 4(g)(i) shows that the local strain rate, s^2 , is nearly zero inside this roller. The corresponding C remains relatively smooth and has a local maximum at the centre of the roller (cf. figure 4b(ii) (blue) and figure 4g(iii) at $x \simeq 76$).

Thus, the accumulation of bubbles in sheets can be attributed to the development of the bubble concentration gradients along the directions of stretching and contraction of the fluid straining motions inside the roller. It is well known (Ottino 1990) that

advection of a non-uniform scalar field decreases the scalar gradients in the direction of stretching (for positive strain rate), and increases the gradients in the direction of contraction (negative strain rate); hence, the sheet-like patterns of the scalar concentration. Now, the bubbles added-mass inertia causes their preferential accumulation in the high-ensrophy regions of the flow (e.g. the centres of ω_y -rollers). On the other hand, since the bubble response time is relatively small, $\tau_b \ll 1/\omega_0 = 1$, the bubble velocity to the zeroth order in $(\tau_b\omega_0)$ equals the sum of the fluid velocity and the terminal velocity, i.e. $V_i \simeq U_i + W\delta_{iz} + O(\tau_b\omega_0)$. Therefore, similar to the passive scalar behaviour, the bubble concentration gradients are also reduced in the direction of stretching, and increased in the direction of contraction in the high-strain flow region inside the roller (e.g. the roller located at $x \simeq 60$ at time $t = 155$ (figures 4a(ii) and 4g(i)), and the same roller at $x \simeq 70$ and $t = 160$ in figures 4a(iii) and 4g(ii)). As a result, the sheets of increased C are created in the rollers with high local strain rate (cf. figures 4a, 4b(iii) and 4g(iii),(iv)).

It is important to note that the transport equation for the bubble-phase concentration, $C(\mathbf{r}, t)$, is identical to the equation of the instantaneous probability distribution function (PDF) of the physical coordinate of a single bubble, $\mathbf{r}(t)$. Therefore, (2.8) can be considered also as the equation for the instantaneous PDF of the bubble location. Thus, the development of C -sheets corresponds to the spatial oscillations of the instantaneous PDF of the location of a single bubble in the flow field of a roller having two local vorticity maxima and an enhanced strain-rate between the maxima (figures 4a, 4b, 4g). Similar oscillations of the bubble concentration are created in the Stuart vortex test case discussed above in §3. The physical explanation of these spatial oscillations is that the trajectories of individual bubbles can be complicated in the vicinity of hyperbolic stagnation points in the regions of high strain rate (Ottino 1990). Figure 4(g) shows clearly the correlation between the spatial locations of the C -sheets and the maxima of s^2 . The figure shows also that thickness of the C -sheets typically is of the order of the characteristic lengthscale of s^2 .

In order to examine the spatial resolution of the sheet-like structure of bubble concentration and the carrier flow ω_y -vorticity in the z -direction, we display in figure 4(h) the profiles of $\omega_y(z)$ and $C(z)$ along the cross-section $x = 68$ of the flow field shown in figures 4(a) and 4(b)(iii). The locations of the grid nodes in the z -direction are denoted by symbols. The figure shows that the width of the regions of increased magnitudes of ω_y -vorticity and C is typically more than three grid spacings. Thus, both the ω_y -layers and C -sheets are resolved in our DNS. We also performed a test of the grid-dependence of a two-dimensional numerical solution for both the carrier flow and the bubble phase (see Appendix B). The test shows that reducing both the grid spacing and the timestep by factor $\frac{4}{3}$ essentially reproduces flow obtained from a simulation with the mesh (i.e. in the x - and z -directions) and timestep used in the DNS of the three-dimensional bubble-laden SDML. The maximum difference between the corresponding results is of the order of 4%. Therefore, we confirm that the oscillations in the concentration profile $C(z)$ exceeding 4% of the absolute maximum (i.e. $0.06\alpha_0$) in figure 4(h) are physical (i.e. not created artificially), and the C -sheets are adequately resolved by the LEM solver.

4.1.2. Average fields

In this section we examine the distributions of the fluid velocity and bubble concentration, averaged both in space and time, and their variance. We also use the average velocity profile to evaluate the ML average vorticity thickness.

An average of a field f (where f denotes the fluid velocity or bubble concentration)

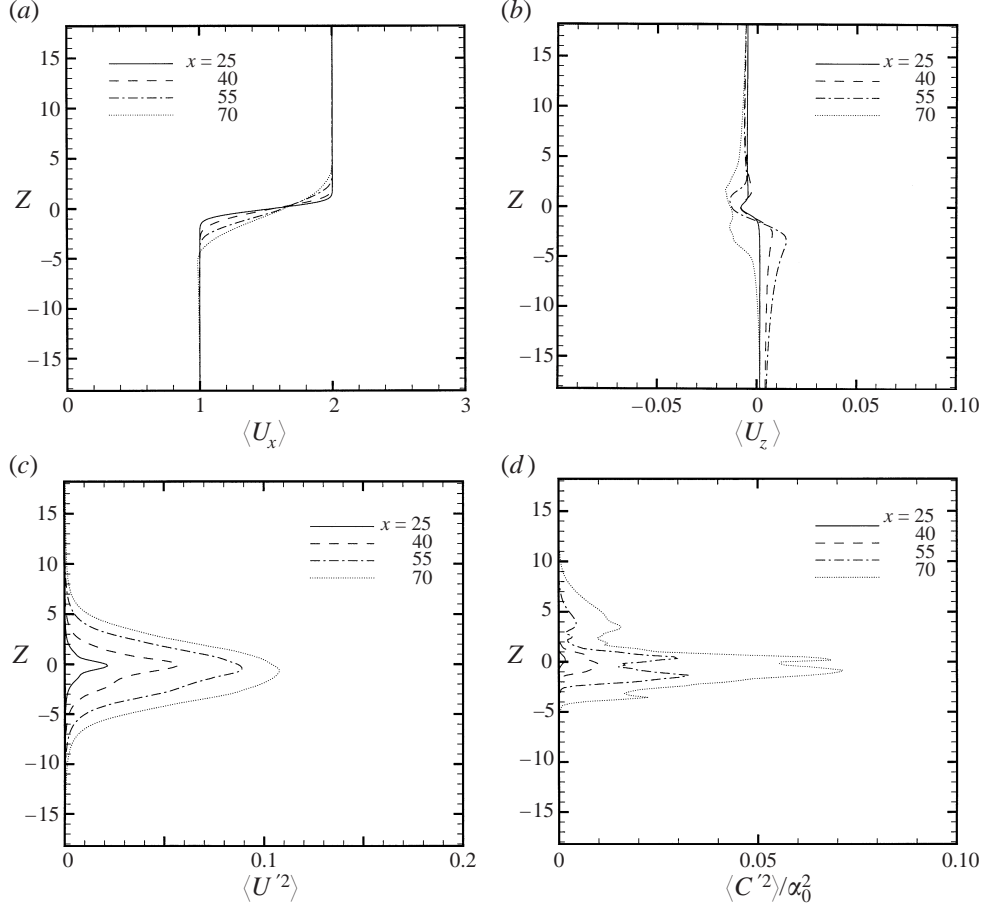


FIGURE 5. (a) Average fluid velocity x -component profile, $\langle U_x \rangle(z)$, at different streamwise locations. (b) Average fluid velocity z -component profile, $\langle U_z \rangle$, at different streamwise locations. (c) Velocity variance profile, $\langle U'^2 \rangle$, at different streamwise locations. (d) Concentration variance profile, $\langle C'^2 \rangle / \alpha_0^2$, at different streamwise locations. $Re = 400$ (one-way, 3D)

is evaluated in two steps. First, a spatial line-average in the spanwise direction, $\langle f(x, z, t) \rangle_y$, is evaluated at a given point in the (x, z) -plane and time t via summation of the instantaneous flow fields $f(x, y_j, z, t)$ at the grid points y_j , $j = 1, \dots, N_y$, ($N_y = 32$). Then, a time average, $\langle f(x, z) \rangle$, is obtained via summation of the line-averaged flow fields $\langle f(x, z, t_n) \rangle_y$ obtained at consecutive times $t_n = n$, $n = 81, 82, \dots, 160$. Thus, the spanwise time average field, $\langle f(x, z) \rangle$, is evaluated according to:

$$\langle f(x, z) \rangle = \frac{1}{N_y} \frac{1}{80} \sum_{m=1}^{N_y} \sum_{n=81}^{160} f(x, z, y_m, t_n). \quad (4.5)$$

The average fields are obtained for $t \geq 80$ because the time interval $\Delta t = 20$, measured from the time of injection of the bubble-phase, $t = 60$, is large enough compared to both the characteristic eddy turnover time of the rollers (estimated as $1/\omega_0 \simeq 1$) and the bubble response time, $\tau_b = 0.05$. Thus, the bubble-phase motion can be regarded as nearly stationary for $t \geq 80$.

Figures 5(a) and 5(b) show the average fluid velocity components, $\langle U_x \rangle$ and $\langle U_z \rangle$, evaluated according to (4.5). The $\langle U_x \rangle$ profiles have the typical tanh-shape and

become more smooth (i.e. the gradient $\partial\langle U_x \rangle / \partial z$ is reduced) owing to the growth of ML lateral thickness with the downstream distance. The $\langle U_z \rangle$ profiles have positive and negative asymptotic values at large negative and positive z , respectively, owing to the entrainment of the irrotational fluid into the ML core. $\langle U_z \rangle$ changes its sign in the ML core region, and the shape of the profile depends on the streamwise location. For example, at $x = 25, 40$ and 55 , $\langle U_z \rangle$ changes its sign within the zone $-3 \leq z \leq 3$ owing to the entrainment of the fluid into the spanwise rollers from the high- and low-speed streams (cf. figure 1 of Dimotakis 1986). At $x = 70$, the fluid moves preferentially downwards, so that $\langle U_z \rangle$ is negative in the ML core region ($-5 \leq z \leq 5$), indicating a pronounced asymmetry of the layer in the z -direction.

Figures 5(c) and 5(d) show the variance of the fluid velocity, $\langle U'^2 \rangle$, and that of the bubble concentration, $\langle C'^2 \rangle$, computed from:

$$\langle U'^2 \rangle = \sum_{i=x,y,z} \langle (U_i - \langle U_i \rangle)^2 \rangle \quad (4.6)$$

and

$$\langle C'^2 \rangle = \langle (C - \langle C \rangle)^2 \rangle. \quad (4.7)$$

As expected, the fluid velocity variance increases with distance downstream owing to the growth of the fundamental and subharmonic instability modes which are responsible for the spanwise vortex roll-up and pairing. At any x location, the $\langle U'^2 \rangle(z)$ profile has its maximum in the ML core region ($|z| < 1$), and tends to zero in the irrotational fluid region ($|z| > 5$). A nearly similar behaviour by the concentration variance is observed. However, the $\langle C'^2 \rangle$ -profile becomes more wrinkled farther downstream owing to the bubble preferential accumulation in the spanwise rollers. Note also that a secondary peak of $\langle C'^2 \rangle$ is created at the ML upper edge (figure 6d, $z \simeq 3.5$ and streamwise locations $x = 55$ and 70). This peak can be attributed to the concentration fluctuations caused by the bubble accumulation in the pairs of counter-rotating rib vortices, joining the tops of the spanwise rollers and moving upwards owing to their self-induction (figures 4a to 4f). Another source of the concentration fluctuations at the upper edge of the ML is the reduction of the concentration at the periphery of the (ω_y) rollers owing to the bubble preferential accumulation in the rollers centres.

Figures 5(a)–5(d) show the growing ML asymmetry in the z -direction, since the z -coordinate of the inflection point of $\langle U_x \rangle$ profile (figure 5a), and the maxima of the variances, $\langle U'^2 \rangle$ and $\langle C'^2 \rangle$, are shifted towards negative z for $x \geq 55$. This is in agreement with the results of other studies by Dimotakis (1986), Koochesfahani & Dimotakis (1986) and Lowery & Reynolds (1986) which show the bending of ML towards the low-speed stream and the preferential entrainment of the fluid from the high-speed stream.

In order to characterize the streamwise development of the $\langle U_x \rangle$ velocity profile and the flow asymmetry, we evaluate the average ML vorticity thickness, δ_ω , and ML deflection parameter, $\Delta\Pi$, defined for each x as:

$$\delta_\omega = \left(\frac{d\langle U_z \rangle}{dz} \right)_{max}^{-1} \quad (4.8)$$

and

$$\Delta\Pi = \Pi^+ + \Pi^- = \int_0^{z_*} (\langle U_x \rangle - U_{ref}) dz + \int_{-z_*}^0 (\langle U_x \rangle - U_{ref}) dz, \quad (4.9)$$

where $U_{ref}(z)$ is the reference velocity (2.1) and $z_* = 4 \ln 95 \simeq 18.22$ (obtained from

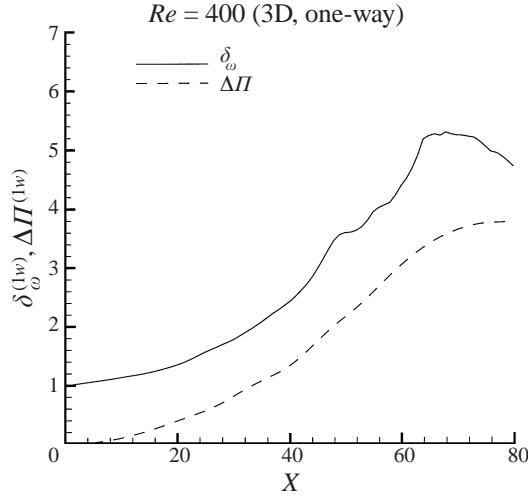


FIGURE 6. Streamwise development of the average vorticity thickness, δ_ω , and the layer deflection parameter, $\Delta\Pi$.

(2.13) for $\xi = 1 - 2/N_z$, $N_z = 96$). The quantities Π^\pm represent the modifications of the fluid mass flux in the high- and low-speed streams, caused by the ML streamwise development and the entrainment of the irrotational fluid into the ML core. Note that $\Pi^+ = -\Pi^-$ and $\Delta\Pi \equiv 0$ in the TDML (which is periodic in the x -direction). In that case, the average streamwise velocity profile is an anti-symmetric function of z with respect to its inflection point, $z = 0$. In contrast, in our case of SDML, the rate of entrainment of the irrotational fluid from the high-speed stream is larger than that from the low-speed stream, i.e. $\Pi^+ > -\Pi^-$, and $\Delta\Pi > 0$.

Figure 6 shows that, as expected, both δ_ω and $\Delta\Pi$ grow with downstream distance, for $0 \leq x \leq 62$. This is in agreement with the results of other studies by Dimotakis (1986), Koochesfahani & Dimotakis (1986) and Lowery & Reynolds (1986), indicating that the growth of the ML vorticity thickness is accompanied by an increase of the entrained mass flux of the high-speed stream as compared to that of the low-speed stream. For larger x , δ_ω and $\Delta\Pi$ saturate, and δ_ω is even slightly reduced for $x > 72$. Winant & Browand (1974) showed that the growth of the ML vorticity thickness is governed by the vortex roll-up, the growth of the first subharmonic mode and the pairing of the spanwise rollers. Thus, the saturation of the growth of the ML vorticity thickness and deflection parameter is caused by the suppression of the fundamental mode and the saturation of the first subharmonic mode. A similar streamwise development of δ_ω was observed in numerical studies by Lowery & Reynolds (1986).

4.2. Two-way coupling effects

Now we present the results of DNS of the bubble-laden three-dimensional SDML with two-way coupling for a reference bubble volume fraction $\alpha = 0.01$. All other flow parameters are equal to those in the one-way coupling case discussed above. The two-way coupling source term (i.e. the last term on the right-hand side of (2.5)) is set equal to zero for time $t < 80$. Thus, the flow field at time $t = 80$ is identical to that in the one-way coupling case. For $t \geq 80$, the source term is computed at every timestep. The simulation is continued until time $t = 160$.

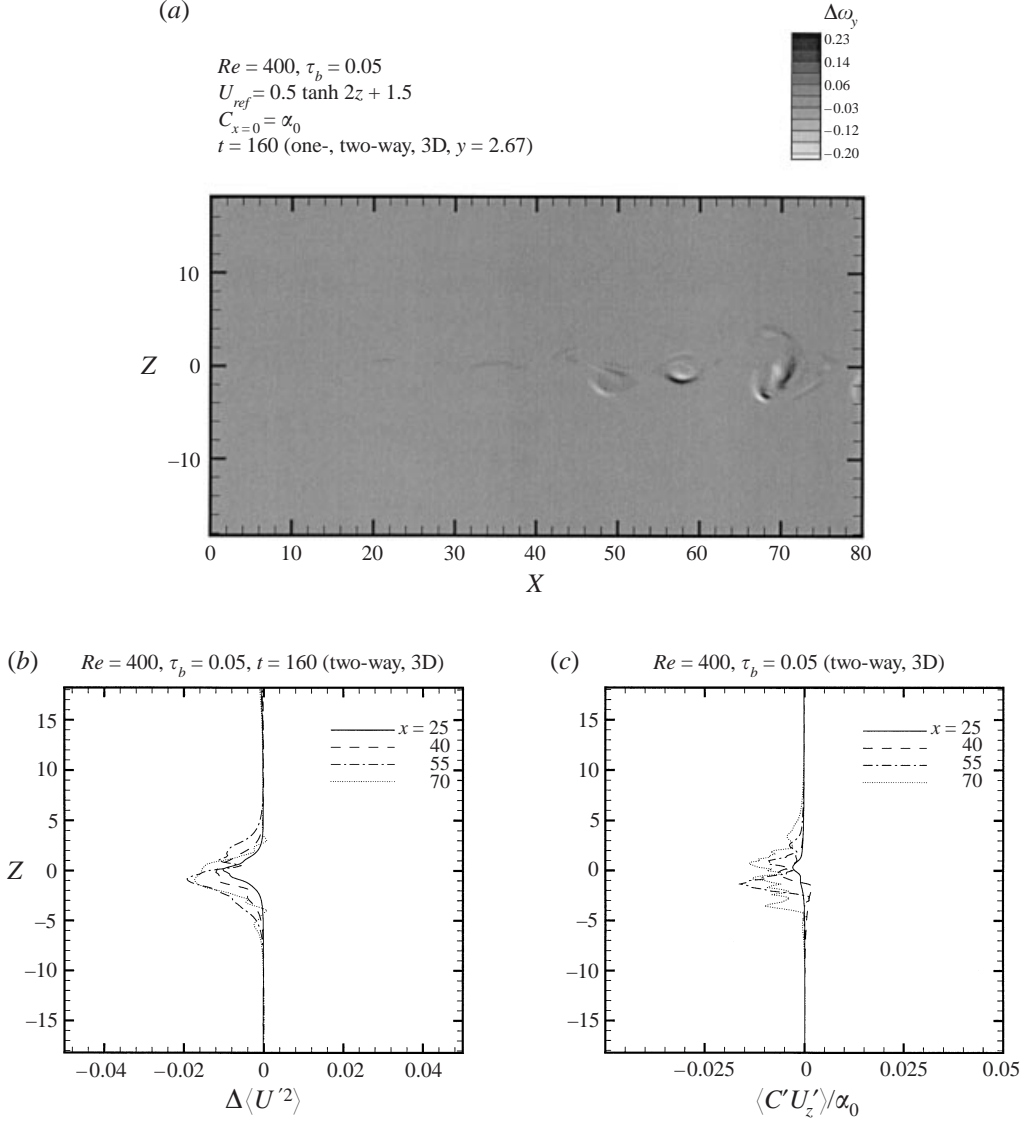


FIGURE 7. (a) Vorticity difference contours, $\Delta\omega_y = \omega_y^{(2w)} - \omega_y^{(1w)}$, in the (x, z) -plane at $y = 2.67$ of the three-dimensional SDML at time $t = 160$. The bubble reference volume fraction $\alpha_0 = 0.01$. (b) Modification of the fluid velocity variance, $\Delta\langle U'^2 \rangle = (\langle U'^2 \rangle_{2w} - \langle U'^2 \rangle_{1w}) / \langle U'^2 \rangle_m$, at different streamwise locations. (c) Average buoyancy flux profile, $\langle C'U'_z \rangle / \alpha_0$, at different streamwise locations.

Figure 7(a) shows the contours of the difference between the values of the instantaneous spanwise vorticity (4.3) in the two-way and one-way coupling cases, $\Delta\omega_y = \omega_y^{(2w)} - \omega_y^{(1w)}$, in an (x, z) -plane at $y = 2.67$ and time $t = 160$. The figure shows that the modification of the flow vorticity is most pronounced near the centres of the spanwise rollers located at $x \simeq 50, 60$ and 70 (figure 4a(iii)), where $\Delta\omega_y$ is maximum and the bubble concentration is increased owing to the bubble preferential accumulation. The two-way coupling creates regions of positive $\Delta\omega_y$ inside the rollers neighbouring regions of negative $\Delta\omega_y$. A similar dipole-like modification of the carrier flow vorticity by the bubbles was observed by Ruetsch & Meiburg (1994) in their

numerical simulation of a two-dimensional temporally growing bubble-laden shear layer, using trajectory approach. Our explanation of the dipole-like modification of the vorticity field, $\Delta\omega_y$, is as follows.

The governing equation for the spanwise vorticity (y -component), defined in (4.3), is obtained from (2.5) in the form:

$$\frac{D\omega_y}{Dt} + U_{ref}\partial_x\omega_y = \omega_j\partial_j\tilde{U}_y + \nu\partial^2\omega_y - g\partial_x(C - C_{ref}), \quad (4.10)$$

where summation over $j(= x, y, z)$ is performed in the first term on the right-hand side. The first and second terms on the right-hand side of (4.10) describe the stretching and viscous diffusion of the vorticity, respectively. The last term describes the source of modification of the carrier flow vorticity by the bubbles. This source term is proportional to the negative x -component of the bubble concentration gradient. Now since bubbles accumulate preferentially inside the spanwise (ω_y) rollers, the x -component of the concentration gradient changes its sign in the vicinity of a local concentration maximum. Thus, ω_y is reduced for positive $\partial_x(C - C_{ref})$, and enhanced for negative $\partial_x(C - C_{ref})$, hence, a dipole-like vorticity production by the bubbles (figure 7a). This production of ω_y -vorticity by the bubbles is modified further by the advection, stretching and viscous dissipation of ω_y (cf. (4.10)).

In order to examine the modification of the fluid velocity fluctuations by the bubbles, we plot in figure 7(b) the relative difference of the variance of the fluid velocities in the two-way and one-way coupling cases, as defined in (4.5) and (4.6):

$$\Delta\langle U'^2 \rangle = (\langle U'^2 \rangle_{2w} - \langle U'^2 \rangle_{1w}) / \langle U'^2 \rangle_m, \quad (4.11)$$

normalized by the maximum variance of the velocity (obtained from the $\langle U'^2 \rangle_{1w}$ -profiles for each x -location in figure 5(b)). The figure shows that the variance is reduced, as compared to the one-way coupling case.

The reduction of the fluid velocity variance by the bubbles is caused by the two-way coupling source term in the transport equation of the turbulence kinetic energy (Druzhinin & Elghobashi 1998), $E = 0.5\langle U'^2 \rangle$. This source term equals $g\langle C'U'_z \rangle$, i.e. an average buoyancy flux. We present this flux (with $g = 1$) at different streamwise locations in figure 7(c). The figure shows that $\langle C'U'_z \rangle$ is negative in the ML core region for all x . Thus, the corresponding source term reduces the turbulence kinetic energy in the ML core, as compared to the one-way coupling case (cf. figure 7b).

In order to quantify the influence of the bubbles on the ML streamwise development, we compare the average ML vorticity thickness obtained from $\langle U_x \rangle$ -profiles according to (4.8), in the two-way and one-way coupling cases, $\delta_\omega^{(2w)}$ and $\delta_\omega^{(1w)}$. Figure 8(a) (top) shows the streamwise development of the relative difference $\Delta\delta_\omega = (\delta_\omega^{(2w)} - \delta_\omega^{(1w)}) / \delta_\omega^{(1w)}$. The figure shows that the ML vorticity thickness in the two-way coupling case is reduced for $x \leq 44$, before the first vortex pairing (figure 4a), and is increased for $x \geq 50$, after the first pairing, as compared to the one-way coupling case. The reason for this development of $\Delta\delta_\omega$ will be explained below. This behaviour is also in agreement with the streamwise development of the modification of the average vertical fluid velocity, defined as

$$\Delta\langle U_z \rangle = \langle U_z \rangle_{2w} - \langle U_z \rangle_{1w},$$

and shown in figure 8(b). This figure shows that $\langle U_z \rangle$ is reduced for negative z at $x = 55$ (since $\Delta\langle U_z \rangle$ is negative). Thus, the two-way coupling reduces the entrainment of the irrotational fluid into the ML core for $x \leq 55$.

The reduction of the ML thickness before the streamwise location of the first vortex

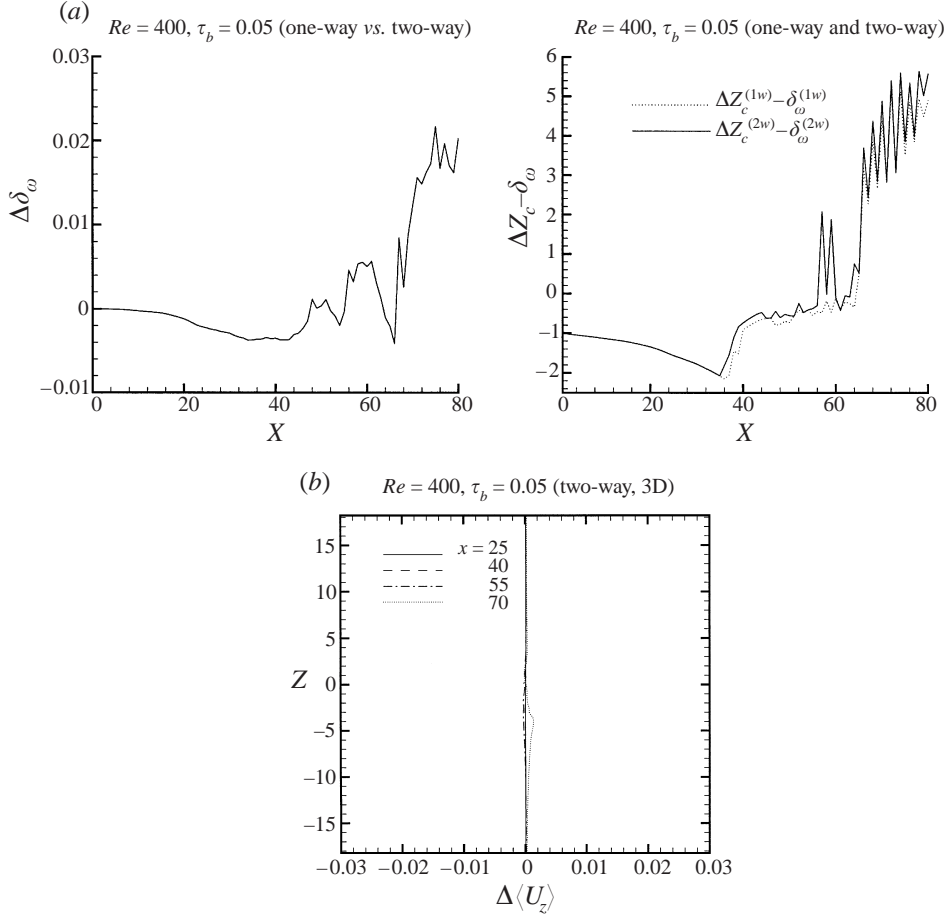


FIGURE 8. (a) Streamwise development of the relative difference of the average vorticity thickness, $\Delta\delta_\omega = (\delta_\omega^{(2w)} - \delta_\omega^{(1w)})/\delta_\omega^{(1w)}$ (top: two- vs. one-way coupling), and the difference of the concentration variance thickness and the average vorticity thickness, $\Delta Z_c - \delta_\omega$ (bottom: one- and two-way coupling). (b) Modification of the z -component of the average fluid velocity, $\langle U_z \rangle_{2w} - \langle U_z \rangle_{1w}$, at different streamwise locations.

pairing ($x \leq 44$, figure 4a) is a result of the suppression of the fluid velocity fluctuations by the bubbles owing to the negative sign of the buoyancy flux (figure 7c). In this region, the growth of δ_ω is caused by the enhancement of the spanwise vorticity which is initially governed by the Kelvin–Helmholtz instability (Michalke 1964). Since the negative buoyancy flux reduces the fluid velocity fluctuations (Druzhinin & Elghobashi 1998), the entrainment of the irrotational fluid into the ML core and the growth of the vorticity thickness are also reduced, as compared to those of bubble-free ML.

Farther downstream, after the first pairing, the growth of δ_ω is governed by the dynamics and pairing of the spanwise rollers in the one-way coupling case (Winant & Browand 1974), and is modified by the dipole-like vorticity production in the two-way coupling case (figure 7a, $x \geq 44$). In this flow region, the bubble-phase concentration becomes strongly non-uniform, and the concentration fluctuations increase with downstream distance, owing to the preferential accumulation of bubbles in the centres of the ω_y -rollers accompanied by the reduction of C in the streaks.

In order to characterize the streamwise development of the bubble concentration in the ML, we evaluate the thickness of the concentration variance distribution, $\Delta z_C(x) = z_2 - z_1$, such that in the interval ($z_2 < z < z_1$), for each streamwise location (x), the concentration variance is larger than 2% of its absolute maximum, $\langle C'^2 \rangle(z_1 < z < z_2) > 0.02 \langle C'^2 \rangle_{max}$, where $\langle C'^2 \rangle_{max} = 0.23\alpha_0^2$ and $0.20\alpha_0^2$ in the one-way and two-way coupling cases, respectively. Figure 8(a) (bottom) shows the streamwise development of the difference ($\Delta Z_C - \delta_\omega$) in the one- and two-way coupling cases. The figure shows that $\Delta Z_C > \delta_\omega$ for $x \geq 60$ for both one-way and two-way coupling. The larger thickness of the concentration variance, ΔZ_C , as compared to δ_ω , is caused by the reduction of the bubble concentration in the streaks at the peripheries of the ω_y -rollers, where the fluid motion is almost irrotational (figure 4b, also figure 3a for the bubble-laden Stuart vortex). Since the fluctuations of the concentration create streamwise gradients, $\partial_x C$, the vorticity production owing to the two-way coupling (cf. (4.10)) occurs not only in the ML core, but also at the peripheries of the ω_y -rollers. This vorticity production widens the ML vorticity distribution and enhances the entrainment of the irrotational fluid into ML core, hence the increase of δ_ω owing to the two-way coupling. The enhancement of the entrainment for $x > 44$, as compared to the bubble-free case, results in a positive mean velocity difference $\Delta \langle U_z \rangle$ (figure 8b, $x = 70$).

The difference ($\Delta Z_C - \delta_\omega$) (solid line in figure 8a) is increased by the two-way coupling because the increased vorticity thickness, which is proportional to the characteristic lengthscale of the spanwise rollers in the ML core, enhances the bubble dispersion as compared to the one-way coupling case (dotted line in figure 8a).

5. Three-dimensional SDML with tanh-profile for inflow bubble concentration

DNS of the bubble-laden three-dimensional SDML with a tanh inflow profile for the bubble concentration (2.4) was performed for the same flow parameters and using the same numerical procedure as in the case of the uniform bubble distribution (§4 above), with both one- and two-way coupling.

5.1. One-way coupling

In the one-way coupling case, all the characteristics of the carrier flow are identical to those presented in §4. Therefore, here we describe only the structure of the bubble concentration field.

Figure 9(a) shows the instantaneous contours of the bubble concentration (in grey scale) in an (x, z)-plane at the same y -location and times as figures 4(a) and 4(b). In the case of the inflow tanh-profile $C_{ref}(z)$ (2.4), the high-speed (upper) stream is devoid of bubbles, and the low-speed (lower) stream is laden with a uniform concentration of bubbles at $x = 0$. As the bubbles are advected downstream and rise vertically owing to buoyancy, they enter the high-speed stream, so that the concentration interface is shifted from the initial location $z \simeq 0$, at $x = 0$, upwards into the high-speed stream ($z > 0$). On the other hand, the downstream development of the spanwise (ω_y) rollers causes the entrainment of the fluid from the upper stream, which is devoid of bubbles, into the ML core. This entrainment is accompanied by the preferential accumulation of bubbles in the centres of ω_y -vortices and the creation of streaks of fluid with increased bubble concentration extending from the braids to the peripheries of the vortices (cf. figure 3c for the bubble-laden Stuart flow). As in the case of a uniform inflow C_{ref} , sheet-like patterns of increased concentration are created owing

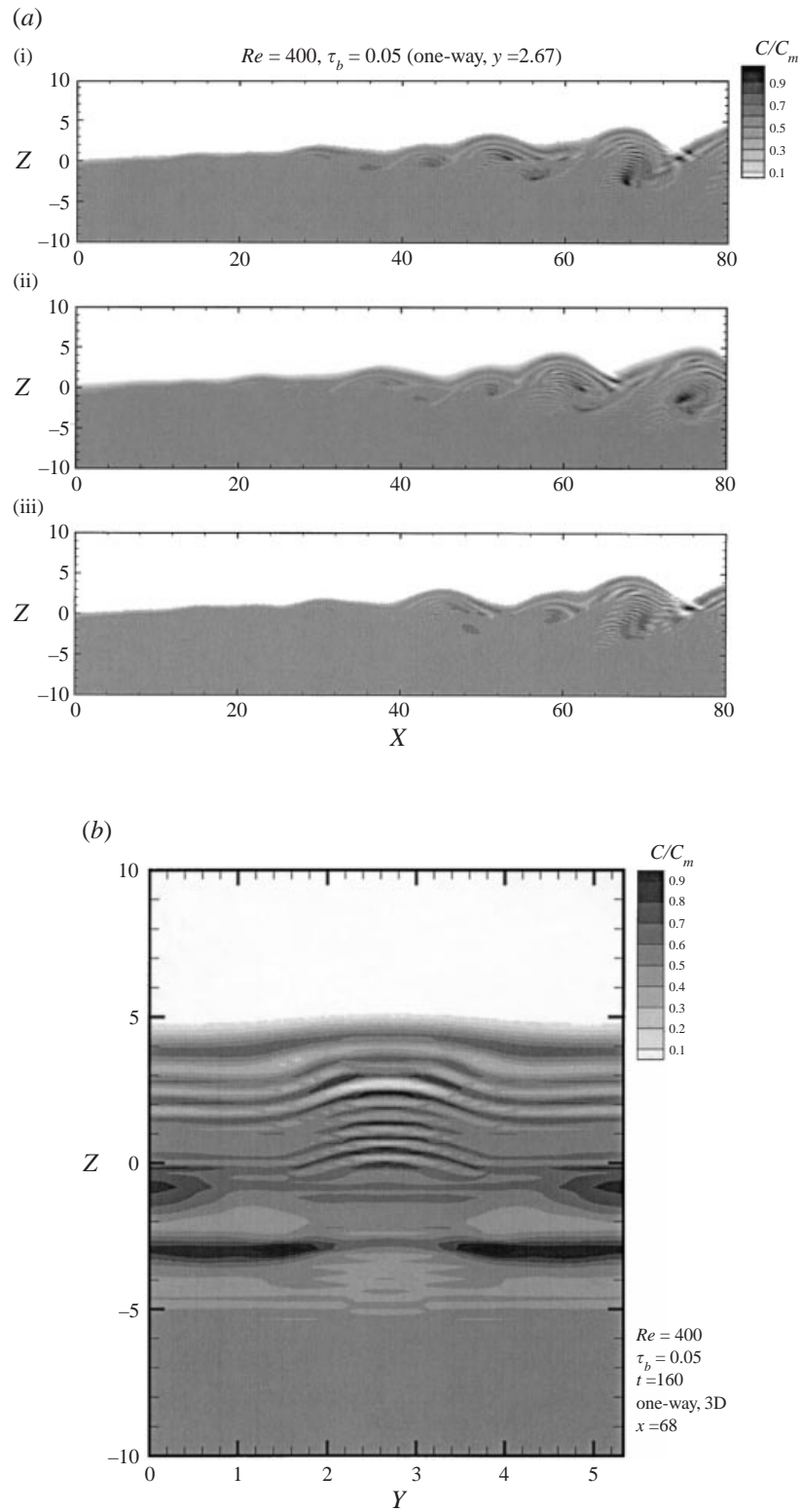


FIGURE 9 (a, b). For caption see facing page.

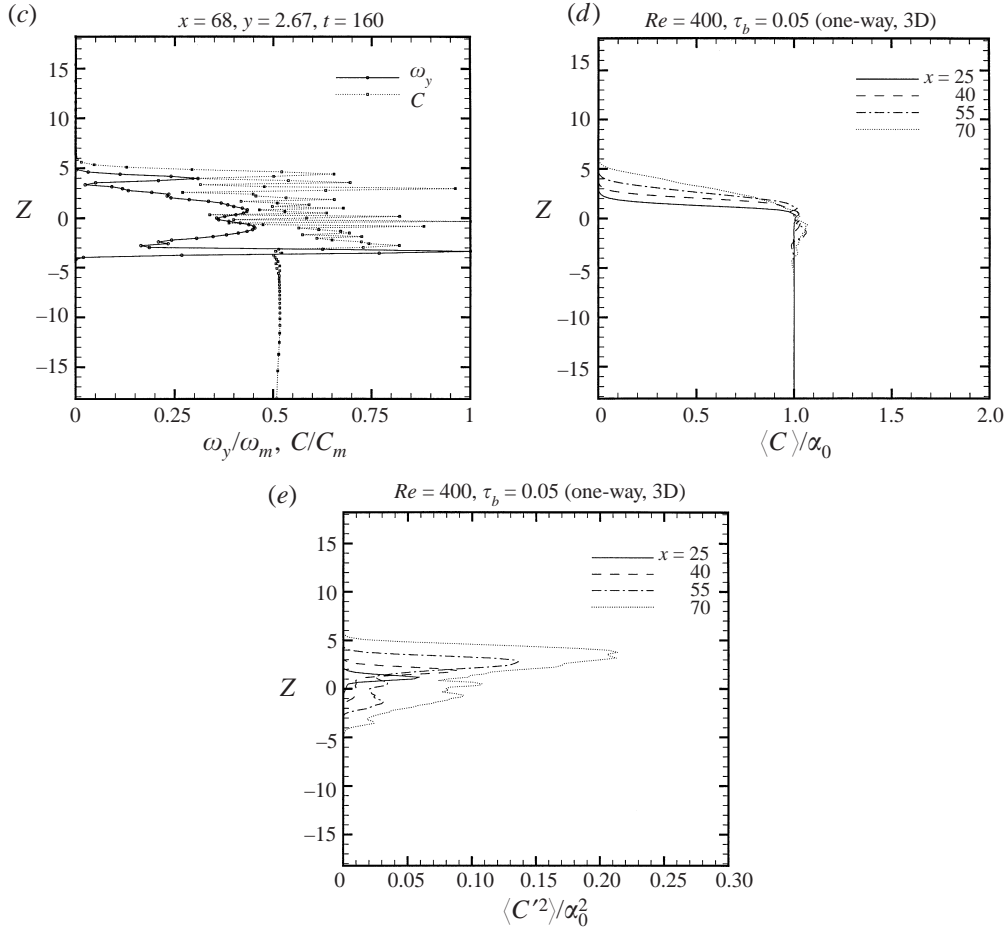


FIGURE 9. (a) Bubble concentration contours in the (x, z) -plane at $y = 2.67$ of the three-dimensional SDML at different times, (i) $t = 150$, (ii) $t = 155$ and (iii) $t = 160$. Concentration maxima are (i) $C_m = 1.86\alpha_0$, (ii) $C_m = 2.01\alpha_0$ and (iii) $C_m = 2.97\alpha_0$, respectively. Inflow bubble concentration $C_{ref} = 0.5\alpha_0(1 - \tanh 2z)$. (b) Bubble concentration contours in the (y, z) -plane at $x = 68$ of the three-dimensional SDML at time $t = 160$. Maximum concentration $C_m = 1.99\alpha_0$; $C_{ref} = 0.5\alpha_0(1 - \tanh 2z)$. (c) z -profiles of the ω_y -vorticity component and bubble concentration, C , normalized by their respective local maximum values, $\omega_m = 0.99$ and $C_m = 1.94\alpha_0$, at $x = 68$, $y = 2.67$ and the same time as figure 9(a). $C_{ref} = 0.5\alpha_0(1 - \tanh 2z)$. (d) Mean concentration profile, $\langle C \rangle/\alpha_0$, at different streamwise locations. Inflow bubble concentration $C_{ref} = 0.5\alpha_0(1 - \tanh 2z)$. (e) Concentration variance profile, $\langle C'^2 \rangle/\alpha_0^2$, at different streamwise locations; $C_{ref} = 0.5\alpha_0(1 - \tanh 2z)$.

to the accumulation of bubbles in the rollers containing two corotating vortices (cf. the rollers at $x \simeq 60$ in figure 9a(ii) and at $x \simeq 68$ in figure 9a(iii); see also figures 4a and 4b). On the other hand, the bubble concentration remains relatively smooth inside the rollers where the flow is dominated by a single ω_y -vortex (cf. figure 4a(ii) at $x \simeq 76$).

The bubble concentration contours in the (y, z) -plane at $x = 68$ and $t = 160$ are presented in figure 9(b). The corresponding ω_x -vorticity field is shown in figure 4(e). Figure 9(b) shows that sheets of increased bubble concentration are created both in the vicinity of the interface located at $z \simeq 5$, and in the core of the spanwise (ω_y)

roller (see figure 4a(iii) at $x \simeq 70$, $z \simeq -3$). The figure shows that the concentration sheets located in the vicinity of the interface ($z \simeq 4$) are distorted by the upward advection of the fluid in the region between the vortices ($y \simeq 2.7$). The figure shows also that the bubbles accumulate in the centres of streamwise (ω_x) vortices (at $y \simeq 1.5$ and $z \simeq -3$).

In order to examine the spatial resolution of the bubble concentration (C) sheets in the z -direction, we display in figure 9(c) the profiles of $\omega_y(z)$ and $C(z)$ along the cross-section $x = 68$. The vorticity profile is identical to that of figure 4(h). Figure 9(c) shows that, as in the case of uniform inflow concentration profile, the typical width of the regions of increased bubble concentration is several (more than four) grid spacings (as, in figure 4h, the locations of the grid nodes in the z -direction are denoted by symbols), so that C -sheets are adequately resolved by the the LEM solver in this case as well. In order to validate further the accuracy of the LEM solver, we performed a grid-dependence test of the corresponding two-dimensional numerical solution (see Appendix B). The test shows that, as in the case $C_{ref} = \alpha_0$, reducing the grid spacing and timestep by factor $\frac{4}{3}$ reproduces the flow obtained from a simulation with the mesh used in the DNS of three-dimensional SDML3D, with the maximum difference of 4%.

Figures 9(d) and 9(e) show the average bubble concentration and its variance profiles obtained at different streamwise locations using the same averaging procedure (4.5) and (4.7) as in the case of uniform C_{ref} . Figure 9(d) shows that, as expected, the upward shift of the concentration interface, which is located at $z = 0$ at the inflow plane ($x = 0$), increases with downstream distance because of the bubbles rising owing to buoyancy. Figure 9(e) shows that, as in the case $C_{ref} = \alpha_0$, the concentration variance grows with the streamwise distance. However, since the bubble concentration is non-uniform at $x = 0$, the concentration variance is significantly larger than that in the case of uniform C_{ref} at all streamwise locations (see figures 5d and 9e), and, as expected, for each x the maximum of $\langle C'^2 \rangle$ occurs at a z -location where the gradient of $\langle C \rangle$ is maximum (cf. figure 9d). Thus, in this case, the growth of the fluctuations of the bubble concentration is governed mainly by the dynamics of the concentration interface and its interaction with the spanwise rollers in the ML core. On the other hand, the preferential accumulation of bubbles in the spanwise rollers creates secondary peaks of $\langle C'^2 \rangle$ located below the C -interface (cf. figures 9d and 9e, see also figures 9a and 9b).

5.2. Two-way coupling

DNS of the bubble-laden three-dimensional SDML with a tanh-profile for the inflow bubble concentration and two-way coupling has been performed for the same reference bubble volume fraction ($\alpha = 0.01$), as in the case of uniform inflow concentration profile, $C_{ref} = \alpha_0$. All other parameters of the carrier flow and the bubble phase are equal to those in the one-way coupling case discussed above.

As was mentioned in §2, the conservation equation for the carrier fluid momentum (2.5) is analogous to that of a stratified fluid with density $(1 - C)\rho_f$. Therefore, in the flow region where the bubble preferential accumulation is not pronounced (i.e. before the location of the first vortex pairing, $x \leq 44$), the effect of the bubbles on the carrier flow is analogous to that of an unstably stratified flow considered by Druzhinin & Elghobashi (1998).

We quantify the two-way coupling effects by evaluating the modification of the fluid velocity variance, $\Delta \langle U'^2 \rangle$ using (4.11) (figure 10a) and the ML average vorticity thickness, $\Delta \delta_\omega = (\delta_\omega^{(2w)} - \delta_\omega^{(1w)}) / \delta_\omega^{(1w)}$ (figure 10b).

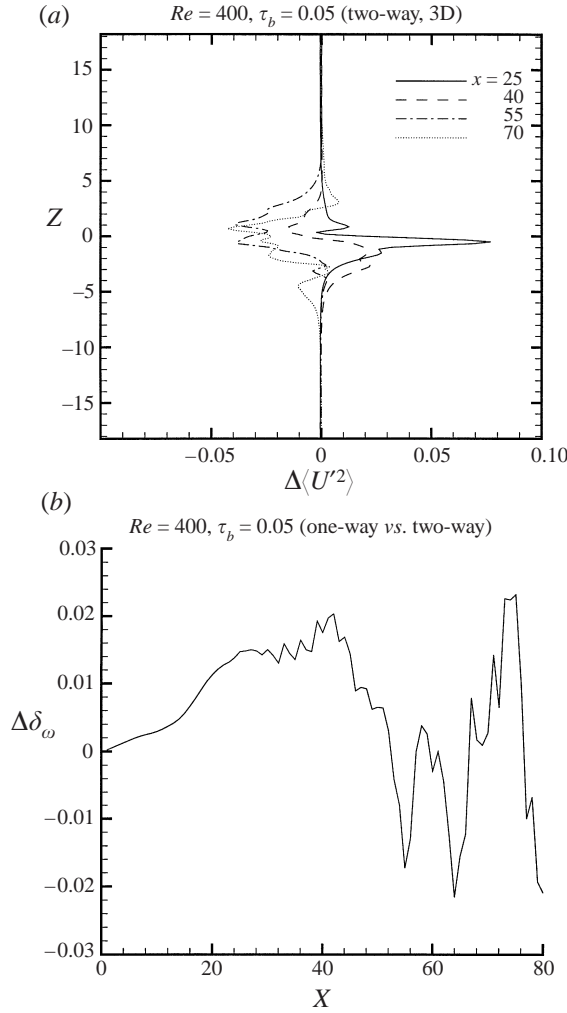


FIGURE 10. (a) Modification of the fluid velocity variance, $\Delta\langle U'^2 \rangle = (\langle U'^2 \rangle_{2w} - \langle U'^2 \rangle_{1w}) / \langle U'^2 \rangle_m$, at different streamwise locations; $C_{ref} = 0.5\alpha_0(1 - \tanh 2z)$. (b) Streamwise development the relative difference of the average vorticity thickness, $\Delta\delta_\omega = (\delta_\omega^{(2w)} - \delta_\omega^{(1w)}) / \delta_\omega^{(1w)}$ (two- vs. one-way coupling); $C_{ref} = 0.5\alpha_0(1 - \tanh 2z)$.

Figure 10(a) shows the profiles of $\Delta\langle U'^2 \rangle$ at four streamwise locations. The figure shows that, as expected, the fluid velocity fluctuations are increased by the bubbles in the region $x \leq 44$, before the location of the first vortex pairing. This enhancement of $\langle U'^2 \rangle$ is a direct consequence of the influence of the unstable stratification due to the inflow tanh-profile of the bubble concentration, $C_{ref}(z)$, (2.4). Increasing the fluid velocity fluctuations is associated with a faster growth of the spanwise vortices and the ML vorticity thickness, as compared to the bubble-free flow. Figure 10(b) shows that, as expected, $\Delta\delta_\omega > 0$ for $x \leq 44$.

Since the spanwise rollers grow with the downstream distance owing to vortex pairings, the structure of the bubble concentration field becomes more complex owing to the entrainment of the fluid that is devoid of bubbles from the upper stream into the ML core, as well as the preferential accumulation of bubbles in the ω_y -rollers. On

the other hand, since the bubbles rise owing to buoyancy, the concentration interface is shifted upwards and is located above the ML core (the region $-5 < z < 2$ where the fluid velocity variance, $\langle U'^2 \rangle$, is larger than half of its maximum at each x -location, see figure 5(c) for $x = 55, 70$). Thus, farther downstream ($x \geq 44$) $\langle C \rangle$ is almost uniform in the ML core (see figures 4a, 9d and 5c). As a result, the fluid velocity fluctuations are reduced by the two-way coupling for $x \geq 44$, similar to the case of the uniform inflow bubble distribution.

Figure 10(b) shows that for $x \geq 44$ the modification of the ML vorticity thickness is quite irregular. The growth of $\Delta\delta_\omega$ in this region is governed by the effects of the concentration gradients on the vorticity production in the sheets of increased C (cf. (4.10)).

6. Conclusions

We have presented the results of direct numerical simulation (DNS) of a three-dimensional spatially developing forced mixing layer laden with small spherical bubbles. The volume fraction of the dispersed bubbles is assumed to be small enough to enable us to neglect bubble–bubble interactions, but large enough to influence the carrier fluid motion. The no-slip condition for the fluid velocity at the bubble surface is assumed. The bubble Reynolds number is less than 1 throughout the simulation. The two-fluid formulation (TF) is used (Druzhinin & Elghobashi 1998), where the bubble phase is treated as a continuum characterized by its velocity and concentration (or volume fraction). TF is implemented in DNS via a Lagrangian–Eulerian mapping (TF-LEM) solver.

DNS of a bubble-laden three-dimensional SDML has been performed with both one- and two-way coupling. Forcing at the inflow plane is used to induce the roll-up of the spanwise vorticity and vortex pairing, and the development of pairs of streamwise counter-rotating vortices, as proposed by Lowery & Reynolds (1986). Bubbles are injected into the carrier flow when the initial flow field and transient fluid motions are ‘washed out’ of the computational domain, and the flow is nearly stationary. We consider two different inflow profiles of the bubble concentration ($C_{ref}(z)$): a uniform profile and a tanh-profile. In the latter case, the high-speed (upper) stream is devoid of bubbles and the low-speed (lower) stream is uniformly laden with bubbles at the inflow plane.

In order to validate our numerical procedure and the LEM solver, we have performed simulations of a bubble-laden Stuart vortex flow with one-way coupling, with both uniform and tanh initial distributions of bubbles, and negligible viscous effects. We also performed a grid dependence test using our numerical procedure for the simulation of a two-dimensional bubble-laden SDML, for both uniform and tanh inflow distributions of bubbles (C_{ref}). The results show that our numerical procedure satisfactorily resolves both the carrier flow dynamics and the bubble-phase structure.

The numerical results show that three-dimensional-patterns of increased concentration of bubbles, C , are created owing to their preferential accumulation in the coherent vortex structures of three-dimensional SDML (spanwise rollers and streamwise ribs). In particular, C is increased in the centres of ω_y -rollers and reduced in the streaks at the periphery of the rollers and in the braid regions between the rollers and remains uniform in the irrotational region. The results show also that sheets of increased concentration are created inside the rollers consisting of two corotating ω_y -vortices (see figures 4a, b). These sheets occur owing to the growth of the concentration gradients

caused by the advection of bubbles in the high-strain region between the vortices. In the case of the tanh-profile of C_{ref} , the concentration sheets are created also owing to the entrainment of the fluid devoid of bubbles from the high-speed stream into the ML core (figure 9a).

It is important to note that the transport equation for the bubble-phase concentration, $C(\mathbf{r}, t)$, is identical to the equation of the instantaneous probability distribution function (PDF) of the physical coordinate of a single bubble, $\mathbf{r}(t)$. Therefore, (2.8) can be considered also as the equation for the instantaneous PDF of the bubble location. Thus, the development of C -sheets corresponds to the spatial oscillations of the instantaneous PDF of the location of a single bubble in the flow field of a roller having two local vorticity maxima and an enhanced strain rate between the maxima (figures 4a, b, g). The physical explanation of these spatial oscillations is that the trajectory of a single bubble in such a roller can be quite complicated in the vicinity of hyperbolic stagnation points in the regions of high strain rate (Ottino 1990). Figure 4(g) shows clearly the correlation between the spatial locations of the C -sheets and the maxima of s^2 .

DNS of the bubble-laden three-dimensional SDML with two-way coupling was performed with a bubble reference volume fraction 0.01 and the same boundary and initial conditions as in the one-way coupling case.

The DNS results and the analysis of the instantaneous two-way coupling source term in the equation of the spanwise (ω_y) vorticity show that bubbles modify the ω_y -vorticity field in a dipole-like manner, creating neighbouring regions of enhanced and reduced vorticity.

The results obtained for the uniform inflow profile of C_{ref} show that the fluctuations of the fluid velocity in the ML core are reduced by the two-way coupling at all streamwise locations x , as compared to those of bubble-free ML. The results also show that the ML average vorticity thickness in the two-way coupling case is reduced for $x \leq 44$, before the first vortex pairing (figure 4a), and increased for $x \geq 44$, after the first pairing, as compared to the one-way coupling case. The reduction of the ML thickness before the streamwise location of the first vortex pairing ($x \leq 44$, figure 8a) is a result of the suppression of the fluid velocity fluctuations by the bubbles owing to the negative sign of the buoyancy flux (figure 7c). In this region, the growth of δ_ω is caused by the enhancement of the spanwise vorticity which is initially governed by the Kelvin–Helmholtz instability (Michalke 1964). Since the negative buoyancy flux reduces the fluid velocity fluctuations (Druzhinin & Elghobashi 1998), the entrainment of the irrotational fluid into the ML core and the growth of the vorticity thickness are also reduced, as compared to those of bubble-free ML. Farther downstream, after the first pairing, the bubble concentration becomes strongly non-uniform, and the concentration fluctuations increase with downstream distance, owing to the preferential accumulation of bubbles in the centres of the ω_y -rollers accompanied by the reduction of C in the streaks. Since the fluctuations of the concentration create non-zero streamwise gradients of C , the vorticity production due to the two-way coupling occurs not only in the ML core, but also at the peripheries of the ω_y -rollers. This vorticity production widens the ML vorticity distribution and enhances the entrainment of the irrotational fluid into the ML core, hence the increase of δ_ω owing to the two-way coupling.

The results obtained for the inflow tanh-profile of C_{ref} show that both the fluid velocity fluctuations and the ML vorticity thickness are increased by the two-way coupling upstream the location of the first vortex pairing owing to the ‘unstable’ inflow stratification of the bubbles (Druzhinin & Elghobashi 1998). However, the velocity

fluctuations are reduced and the growth of the ML thickness becomes irregular farther downstream, as the location of the concentration interface (i.e. the maximum of the gradient of $\partial C/\partial z$) is shifted upwards owing to the bubbles rise by buoyancy.

A typical run for the three-dimensional SDML, with one-way or two-way coupling, for dimensionless time $0 \leq t \leq 160$ takes less than 5 CPU-hours on a Cray T90.

This work was supported by ONR grant number N00014-96-1-0213 and by NASA grant number NAG3-1831. The computations were performed on a Cray T90 located at the Naval Oceanographic Center, Mississippi.

Appendix A. Inflow boundary conditions for the fluid velocity

In order to initialize the roll-up of the spanwise ML vorticity, we apply a forcing to the U_x and U_z components of the inflow velocity. The forcing frequencies are those of the fundamental mode and its first and second subharmonics (Lowery & Reynolds 1986), $\Omega_0 = 4/3$, $\Omega_1 = 2/3$ and $\Omega_2 = 1/3$. The forcing at the subharmonic frequencies speeds up the pairing of the spanwise rollers. The resulting velocity components of this forcing are:

$$U_x^f(z, t) = U_0 \operatorname{Re} \left\{ \sum_{n=0}^{n=2} \hat{U}_{nx}(z) \exp[-i(\Omega_n t + \phi_n)] \right\}, \quad (\text{A } 1)$$

$$U_z^f(z, t) = U_0 \operatorname{Re} \left\{ \sum_{n=0}^{n=2} \hat{U}_{nz}(z) \exp[-i(\Omega_n t + \phi_n)] \right\}, \quad (\text{A } 2)$$

where $\operatorname{Re}\{\dots\}$ denotes the real part of the sums inside the brackets. The random phases (Sandham & Reynolds 1989) ϕ_n are obtained at each timestep as $\phi_n(t + dt) = \phi_n(t) + \eta_n \pi/12$, where η_n is a random number with a uniform distribution ($-1 < \eta_n < 1$). In our simulation, we set $U_0 = 0.02$. The eigenfunctions, \hat{U}_{nx} and \hat{U}_{nz} , and eigenvalue k_n are obtained for each Ω_n ($n = 0, 1, 2$) by solving the two-dimensional Rayleigh equation eigenvalue problem in the form:

$$\left(U_{ref} - \frac{\Omega_n}{k} \right) \left(\frac{d^2 \hat{U}_z}{dz^2} - k^2 \hat{U}_z \right) - \frac{d^2 U_{ref}}{dz^2} \hat{U}_z = 0, \quad (\text{A } 3)$$

$$\hat{U}_x = \frac{i}{k} \frac{d \hat{U}_z}{dz}, \quad (\text{A } 4)$$

where the reference velocity profile $U_{ref}(z)$ is given by (2.1), and the boundary conditions are

$$\hat{U}_z = \exp(\mp kz), \quad z \rightarrow \pm\infty. \quad (\text{A } 5)$$

The eigenvalue problem (A 3)–(A 5) is solved for each Ω_n by a shooting method using a matching condition at $z = 0$. The resulting eigenvalues are $k_0 = 0.8888 - 0.12826i$, $k_1 = 0.4309 - 0.09881i$ and $k_2 = 0.2088 - 0.0582i$.

In addition to the inflow harmonic forcing (A 1) and (A 2), we include a steady flow field created by a pair of counter-rotating Gaussian vortices (Buell & Mansour 1989). The velocity components of this steady flow are:

$$U_y^v = \omega_{0x} r_0^2 z \left[\frac{1 - \exp(-r_1^2/2r_0^2)}{r_1^2} - \frac{1 - \exp(-r_2^2/2r_0^2)}{r_2^2} \right], \quad (\text{A } 6)$$

$$U_z^v = \omega_{0x} r_0^2 \left[\frac{1 - \exp(-r_1^2/2r_0^2)}{r_1^2} (y - y_1) - \frac{1 - \exp(-r_2^2/2r_0^2)}{r_2^2} (y - y_2) \right], \quad (\text{A } 7)$$

where ω_{0x} and r_0 are the core vorticity and radius, respectively, and

$$r_{1,2} = [z^2 + (y - y_{1,2})^2]^{1/2}. \quad (\text{A } 8)$$

In our DNS, we set the vortex core locations at $y_1 = \frac{8}{3} \simeq 2.333$ and $y_2 = 3$. The dimensionless core vorticity and radius are prescribed as $\omega_{0x} = 0.03$ and $r_0 = 0.5\delta_{\omega 0}$, where the ML initial vorticity thickness $\delta_{\omega 0} = 1$.

Therefore, the initial distance, in the y -direction, between the centres of the two vortices is equal to 1.333. Since the flow is periodic in the y -direction, the lengthscale of the disturbance, λ_y , is of the order of the length of the computational domain in this direction (which is equal to 5.333). Thus, for the given fundamental mode wavelength ($\lambda_x \simeq 7$, cf. figure 4a, at $x \simeq 30$), the prescribed lengthscale, λ_y , of the spanwise disturbance is nearly equal to $\frac{2}{3}\lambda_x$. This value of λ_y agrees with the available experimental data of Bernal & Roshko (1986), Lasheras *et al.* (1986), Lasheras & Choi (1988) and theory (Pierrehumbert & Widnall 1982).

Therefore, the three velocity components, \tilde{U}_x , \tilde{U}_y and \tilde{U}_z at the inflow plane ($x = 0$) are prescribed to account for the combined effects of the harmonic forcing (A 1) and (A 2) and the steady flow (A 6) and (A 7) created by the counter-rotating Gaussian vortices, according to:

$$\tilde{U}_x = U_x^f(y, z, t), \quad \tilde{U}_y = U_y^v(y, z), \quad \tilde{U}_z = U_z^f(y, z, t) + U_z^v(y, z). \quad (\text{A } 9)$$

Appendix B. Grid-dependence test

Here, we present the results of the simulation of bubble-laden two-dimensional SDML using two different grids: $N_x = 480$, $N_y = 4$, $N_z = 96$ (timestep $\Delta t = \frac{1}{60}$) and $N_x = 640$, $N_y = 4$, $N_z = 128$ (timestep $\Delta t = \frac{1}{80}$). In the first case, the resolution in the x - and z - directions is identical to that in the case of three-dimensional SDML. Although the flow is homogeneous in the spanwise (y) direction, the simulations were performed using the same numerical procedure as three-dimensional SDML.

In the considered (two-dimensional) case, the forcing at the inflow plane ($x = 0$) was applied only to components U_x and U_z of the fluid velocity, and component U_y was set equal to zero. Only time-dependent forcing with components $U_x^f(z, t)$ and $U_z^f(z, t)$ was applied, and the steady components U_y^v and U_z^v (due to the pair of counter-rotating Gaussian vortices) were set equal to zero. In these test simulations, we excluded random phases from the forcing functions, U_x^f and U_z^f . All other flow parameters, boundary conditions and bubble characteristics were the same as in the DNS of three-dimensional SDML.

Figures 11(a)(i), (ii) and 11(b)(i), (ii) compare the contours (in grey scale) of the ω_y -vorticity and of the bubble concentration obtained from the simulations using the two grids, (i) $480 \times 4 \times 96$ and (ii) $640 \times 4 \times 128$, at time $t = 80$ for the tanh-profile of the inflow bubble concentration (2.4). Now, our numerical procedure is second-order accurate both in space and time. Thus, reducing both the distance between the grid points, Δx , and the time step, Δt , each by a factor $\frac{4}{3}$ reduces the numerical error by a factor $\frac{16}{9} \simeq 1.8$ (i.e. by 40%). On the other hand, comparing figures 11(a)(b)(i) and 11(a)(b)(ii) shows that the difference between the magnitudes of the maxima of vorticity and the bubble concentration obtained in the two-dimensional simulations with the two different grids is less than 2% for the vorticity and 4% for the concentration. Thus, we conclude that the numerical diffusion in our simulation

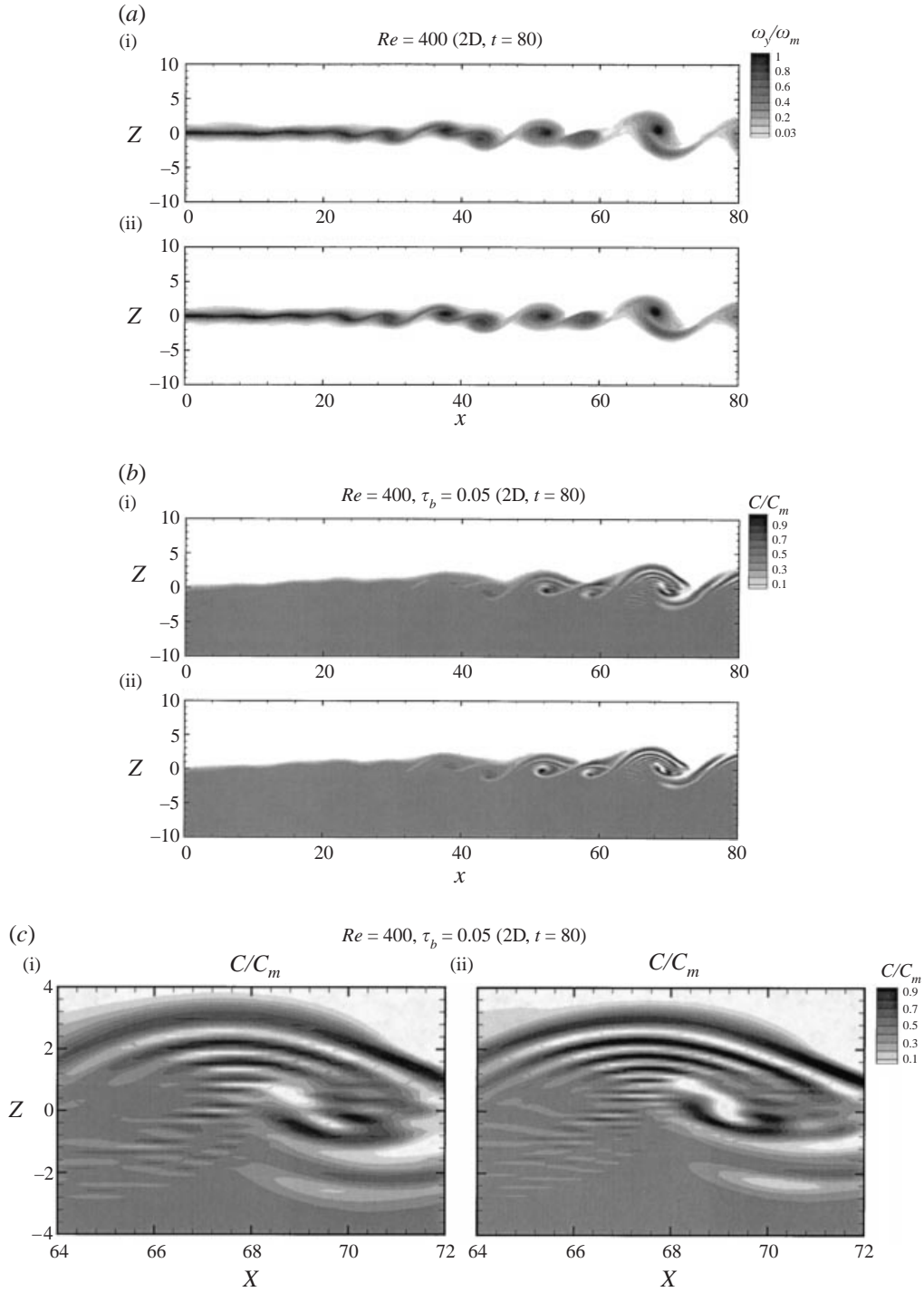


FIGURE 11. (a) Contours of ω_y -vorticity of the two-dimensional SDML in (x, z) -plane at $t = 80$ for two meshes: (i) $480 \times 4 \times 96$ (timestep $\Delta t = \frac{1}{60}$) and (ii) $640 \times 4 \times 128$ ($\Delta t = \frac{1}{80}$). Vorticity maxima are (i) $\omega_m = 1.04$ and (ii) $\omega_m = 1.02$. (b) Contours of the bubble concentration, C/C_m , of the two-dimensional SDML in the (x, z) -plane at $t = 80$ for two different meshes: (i) $480 \times 4 \times 96$ (timestep $\Delta t = \frac{1}{60}$) and (ii) $640 \times 4 \times 128$ ($\Delta t = \frac{1}{80}$). (c) A magnified view of the region ($64 \leq x \leq 72$, $-4 \leq z \leq 4$) of the concentration field of figure 11(b).

is negligible, since increasing the resolution accuracy by 40% causes a negligible correction of the numerical solution. In particular, figures 11(a) and 11(b) show that the simulation with grid $640 \times 4 \times 128$ displays the details of the bubble accumulation in sheets (cf. ω_y -rollers at $x \simeq 70$).

In order to compare in detail the structure of the concentration (C) sheets in two simulations, we select the region of the flow in figure 11(b) ($64 \leq x \leq 72$, $-4 \leq z \leq 4$) and magnify it in figure 11(c). Thus, figure 11(c)(i) is for a grid of $480 \times 4 \times 96$ points, whereas figure 11(c)(ii) is for a grid of $640 \times 4 \times 128$ points.

Both figures 11(c)(i) and 11(c)(ii) show that there are nine sheets of increased concentration (the dark zones) in the region $-0.4 \leq z \leq 3.8$. Note that for a finer grid $640 \times 4 \times 128$ (bottom) the C -sheets are slightly shifted upwards in the vertical (z) direction as compared to the coarser grid $480 \times 4 \times 96$.

Note also that the small-scale C -oscillations are not identical for the two grids in the region $-0.5 \leq z \leq -3$; $64 \leq x \leq 68$ (figures 11(c)(i) and (ii)). However, the grey scale for the contours of C/C_m in figure 11(c) shows clearly that the local maxima in this region are of a smaller magnitude (about 0.4) as compared to the concentration maxima in the C -sheets in the region $z > -0.5$; $67 < x < 68$ whose magnitudes range from 0.7 to 1. Since $C = \alpha_0$ approximately equals the reference concentration for $z < -1$ (since $\tanh(-2) \simeq -0.96$, cf. (4)) and $\alpha_0/C_m \simeq 0.36$ (for $C_m = 2.8\alpha_0$), the magnitude of the instantaneous concentration fluctuations in the region $z < -0.5$ can be evaluated as $C/C_m - \alpha_0/C_m \simeq C/C_m - 0.36$. In the region $z < -0.5$, $x \simeq 66$, $C/C_m \simeq 0.4$, and therefore the magnitude of the C -fluctuations is about $(0.4 - 0.36) = 4\%$ of the reference concentration level, α_0 . Thus, increasing the number of mesh points, from the coarse to the fine grid, by 80%, results in a difference of the concentration maxima in the C -sheets by 4%, while the number of well-pronounced C -sheets remains grid-independent. This result confirms that the formation of C -sheets is a physical phenomenon and not a numerical artifact.

REFERENCES

- BERNAL, L. P. & ROSHKO, A. 1986 Streamwise vortex structure in plane mixing layers. *J. Fluid Mech.* **170**, 499–525.
- BREIDENTHAL, R. 1981 Structure in turbulent mixing layers and wakes using a chemical reaction. *J. Fluid Mech.* **109**, 1–23.
- BROWN, G. L. & ROSHKO, A. 1974 On density effects and large structure in turbulent mixing layers. *J. Fluid Mech.* **64**, 775–816.
- BUELL, J. C. & MANSOUR, N. N. 1989 Asymmetric effects in three-dimensional spatially-developing mixing layers. 7th Symposium on Turbulent Shear Flows, p. 9.2.1 (Stanford University, August 1989).
- CORCOS, G. M. & LIN, S. J. 1984 The mixing layer: deterministic models for a turbulent flow. Part 2. The origin of the three-dimensional motion. *J. Fluid Mech.* **139**, 67–95.
- CORCOS, G. M. & SHERMAN, F. S. 1984 The mixing layer: deterministic models for a turbulent flow. Part 1. Introduction and the two-dimensional flow. *J. Fluid Mech.* **139**, 29–65.
- CROWE, C., CHUNG, J. N. & TROUTT, T. R. 1993 Particle dispersion by organized vortex structures, in *Particulate Two-Phase Flow* (ed. M. C. Roco), p. 626–9. Butterworth–Heinemann.
- CROWE, C. T., GORE, R. A. & TROUTT, T. R. 1985 Particle dispersion by coherent structures in free shear flows. *Part. Sci. Technol.* **3**, 149–158.
- CROWE, C. T., TROUTT, T. R. & CHUNG, J. N. 1996 Numerical models for two-phase turbulent flows. *Ann. Rev. Fluid Mech.* **28**, 11–43.
- CORTESI, A. B., YADIGAROGU, G. & BANERJEE, S. 1998 Numerical investigation of the three-dimensional structures in stably-stratified mixing layers. *Phys. Fluids* **10**, 1449–1473.
- DIMOTAKIS, P. E. 1986 Two-dimensional shear-layer entrainment. *AIAA J.* **24**, 1791–1796.

- DRUZHININ, O. A. 1995 On the two-way interaction in two-dimensional particle-laden flows: the accumulation of particles and flow modification. *J. Fluid Mech.* **297**, 49–76.
- DRUZHININ, O. A. & ELGHOBASHI, S. E. 1998 Direct numerical simulations of bubble-laden turbulent flows using the two-fluid formulation. *Phys. Fluids* **10**, 685–697.
- DRUZHININ, O. A. & ELGHOBASHI, S. E. 1999 A Lagrangian–Eulerian mapping solver for direct numerical simulation of bubble-laden turbulent shear flows using the two-fluid formulation. *J. Comput. Phys.* **154**, 174–196.
- ELGHOBASHI, S. E. 1994 ‘On predicting particle-laden turbulent flows’. *Appl. Sci. Res.* **52**, 309–329.
- HO, C.-M. & HUERRE, P. 1984 Perturbed free shear layers. *Ann. Rev. Fluid Mech.* **16**, 365–424.
- HUSSAIN, A. K. M. F. 1983 Coherent structures and incoherent turbulence. In *Turbulence and Chaotic Phenomena in Fluids* (ed. T. Tatsumi), pp. 453–467. North-Holland.
- KIGER, K. T. & LASHERAS, J. C. 1995 The effect of vortex pairing on the particle dispersion and kinetic energy transfer in a two-phase turbulent shear layer. *J. Fluid Mech.* **302**, 149–178.
- KOOCHESFAHANI, M. M. & DIMOTAKIS, P. E. 1986 Mixing and chemical reactions in a turbulent liquid mixing layer. *J. Fluid Mech.* **170**, 83–112.
- LASHERAS, J. C., CHO, J. S. & MAXWORTHY, T. 1986 On the origin and evolution of streamwise vortical structures in a plane, free shear layer. *J. Fluid Mech.* **172**, 231–258.
- LASHERAS, J. C. & CHOI, H. 1988 Three-dimensional instability of a plane, free shear layer: an experimental study of the formation and evolution of streamwise vortices. *J. Fluid Mech.* **189**, 53–86.
- LAZARO, B. J. & LASHERAS, J. C. 1992a Particle dispersion in the developing free shear layer. Part 1. Unforced flow. *J. Fluid Mech.* **235**, 143–178.
- LAZARO, B. J. & LASHERAS, J. C. 1992b Particle dispersion in the developing free shear layer. Part 1. Forced flow. *J. Fluid Mech.* **235**, 179–221.
- LIN, S. J. & CORCOS, G. M. 1984 The mixing layer: deterministic models for a turbulent flow. Part 3. The effect of plain strain on the dynamics of streamwise vortices. *J. Fluid Mech.* **141**, 139–178.
- LING, W., CHUNG, J. N., TROUTT, T. R. & CROW, C. T. 1998 Direct numerical simulation of a three-dimensional temporal mixing layer with particle dispersion. *J. Fluid Mech.* **358**, 61–85.
- LOWERY, P. S. & REYNOLDS, W. C. 1986 Numerical simulation of a spatially-developing, forced, plane mixing layer. Rep. No. TF-26, Mech. Engng Dept, Stanford University, CA.
- MAGNAUDET, J. J. M. 1997 The forces acting on bubbles and rigid particles. In *Proc. ASME Fluid Engng Div. Summer Meeting*, June, pp. 1–9.
- MARCU, B. & MEIBURG, E. 1996 Three-dimensional features of particle dispersion in a nominally plane mixing layer. *Phys. Fluids* **8**, 2266–2268.
- MARTIN, J. E. & MEIBURG, E. (1994) The accumulation and dispersion of heavy particles in forced two-dimensional mixing layers. I. Fundamental and subharmonic cases. *Phys. Fluids* **6**, 1116–1132.
- MAXEY, M. R. 1987 The motion of small spherical particles in a cellular flow field. *Phys. Fluids* **30**, 1915–1928.
- MICHALKE, A. 1964 On the inviscid instability of the hyperbolic-tangent velocity profile. *J. Fluid Mech.* **19**, 543–556.
- MILLER, R. S. & BELLAN, J. 1999 Direct numerical simulation of a confined three-dimensional gas mixing layer with one evaporating hydrocarbon-droplet-laden stream. *J. Fluid Mech.* **384**, 293–338.
- MOSER, R. D. & ROGERS, M. M. 1993 The three-dimensional evolution of a plane mixing layer: pairing and transition to turbulence. *J. Fluid Mech.* **247**, 275–320.
- OTTINO, J. M. 1990 Mixing, chaotic advection and turbulence. *Ann. Rev. Fluid Mech.* **22**, 207–253.
- PIERREHUMBERT, R. T. & WIDNALL, S. E. 1982 The two- and three-dimensional instabilities of a spatially periodic shear layer. *J. Fluid Mech.* **114**, 59–82.
- RIGHTLEY, P. M. 1995 Bubble dispersion and interphase coupling in a free shear flows. PhD thesis, UC, San Diego.
- ROGERS, M. M. & MOSER, R. D. 1992 The three-dimensional evolution of a plane mixing layer: the Kelvin–Helmholtz rollup. *J. Fluid Mech.* **243**, 183–226.
- RUETSCH, G. R. & MEIBURG, E. 1994 Two-way coupling in shear layers with dilute bubble concentrations. *Phys. Fluids* **6**, 2656–2670.
- SANDHAM, N. D. & REYNOLDS, W. C. 1989 Some inlet plane effects on the numerically simulated

- spatially developing two-dimensional mixing layer. *Turbulent Shear Flows* **6**, pp. 441–447. Springer, New York.
- SCHMIDT, H., SCHUMANN, U. & VOLKER, H. 1984 Three-dimensional, direct and vectorized elliptic solvers for various boundary conditions. Report DFVLR-Mitt. 84-115.
- SCHUMANN, U. & SWEET, R. A. 1988 Fast Fourier transforms for direct solution of Poisson's equation with staggered boundary conditions. *J. Comput. Phys.* **75**, 123–137.
- STUART, J. T. 1967 On finite amplitude oscillations in laminar mixing layers. *J. Fluid Mech.* **29**, 417–440.
- TIO, K.-K., GANAN-CALVO, A. M. & LASHERAS, J. C. 1993 The dynamics of small heavy rigid spherical particles in a periodic Stuart vortex flow. *Phys. Fluids A* **5**, 1679–1693.
- TIO, K.-K., LINAN, A., LASHERAS, J. C. & GANAN-CALVO, A. M. 1993 On the dynamics of buoyant and heavy particles in a periodic Stuart vortex flow. *J. Fluid Mech.* **254**, 671–699.
- WEN, F., KAMALU, N., CHUNG, J. N., CROWE, C. T. & TROUTT, T. R. 1992 Particle dispersion by vortex structure in plane mixing layers. *Trans. ASME: J. Fluids Engng* **114**, 657–666.
- WILHELMSON, R. & ERICKSEN, J. 1977 Direct solution for Poisson's equation in three dimensions. *J. Comput. Phys.* **25**, 319–331.
- WINANT, C. D. & BROWAND, F. K. 1974 Vortex pairing: the mechanism of turbulent mixing-layer growth at moderate Reynolds number. *J. Fluid Mech.* **63**, 237–255.
- YEUNG, P. K. & POPE, S. B. 1988 An algorithm for tracking fluid particles in numerical simulations of homogeneous turbulence. *J. Comput. Phys.* **79**, 373–416.